Journal of Fluids and Structures 66 (2016) 517–542

Contents lists available at ScienceDirect

Journal of Fluids and Structures

journal homepage: www.elsevier.com/locate/jfs

Flow patterns and efficiency-power characteristics of a self-propelled, heaving rigid flat plate

Nipun Arora [a], Amit Gupta [a,*], Sanjeev Sanghi [b], Hikaru Aono [c], Wei Shyy [d]

[a] Department of Mechanical Engineering, Indian Institute of Technology, Hauz Khas, New Delhi 110016, India
[b] Department of Applied Mechanics, Indian Institute of Technology, Hauz Khas, New Delhi 110016, India
[c] Department of Mechanical Engineering, Tokyo University of Science, Katsushika-Ku, Tokyo 125-8585, Japan
[d] Department of Mechanical and Aerospace Engineering, Hong Kong University of Science and Technology, Hong Kong

ARTICLE INFO

Article history:
Received 27 May 2016
Received in revised form
21 July 2016
Accepted 25 August 2016

Keywords:
Reynolds number
Amplitude
Density ratio
Wing–wake interaction
Vortex dipole
Power and efficiency

ABSTRACT

The aim of the present study is to characterize the flow patterns, propulsion efficiency and power requirements associated with a self-propelled-heaving thin flat plate in a quiescent medium. In this regard, a numerical model using a shifting discontinuous-grid and based upon multi-relaxation-time lattice Boltzmann method is developed to probe the resulting aerodynamics. The influence of kinematic parameters namely flapping Reynolds number Re_f $(20-100)$ and plunging amplitude β (0.2–1), and the density ratio ρ^* (10^1-10^2) on forward flight is pursued. Depending on the kinematics, various periodic vortex shedding characteristics of the plunging plate are observed that lead to modification of the angle of attack as a result of wing-wake interaction and downward jet. The presence of strong vortex dipole at the trailing edge with an attached leading edge vortex are factors responsible for maximum thrust generation. A wing-wake interaction which occurs at low β and high Re_f due to weak vortex dissipation and presence of vortex dipole at the trailing edge acting in tandem can lead to achieving high propulsion efficiency. Through surrogate modelling, a set of Pareto-optimal solutions that describe the tradeoff between efficiency and input power for forward flight is presented and offers insight into the design and development of next generation flapping wing micro-air vehicles.

© 2016 Elsevier Ltd. All rights reserved.

1. Introduction

With a dimension span of 15 cm or smaller and flight speed of ~10 m/s or lower, micro-air vehicles (MAVs) operate in low Reynolds number ($\mathrm{Re} < 10^4$) regimes and experience aerodynamic conditions with low lift-to-drag ratios (Shyy et al., 2008, 2013, 2010). These are rapidly evolving as modern defense gadgets for performing surveillance and reconnaissance operations with prerequisites of high-maneuverability, stable hover, vertical take-off/landing capability, swiftness and noiseless locomotion (Shyy et al., 2008, 2013, 2010; Tsai and Fu, 2009; Muller, 2001). While alternative MAV concepts based on fixed wing, rotary wing and flapping wing have been explored, flapping flight has carved its superiority over other designs with excellent maneuverability through space, navigation and control capabilities, stimulating researchers to develop and design this class of MAVs, including Nano-humming bird (Keennon et al., 2012), Microrobot (Fuller et al., 2014; Ma et al., 2015) and Delfly (Croon et al., 2016).

* Corresponding author.
E-mail address: agupta@mech.iitd.ac.in (A. Gupta).

http://dx.doi.org/10.1016/j.jfluidstructs.2016.08.005
0889-9746/© 2016 Elsevier Ltd. All rights reserved.

Nevertheless, as discussed by Shyy et al. (2016) and Chin and Lentink (2016), significant milestones are yet to be achieved for establishing comprehensive predictive capabilities of flapping flight concepts towards development of MAVs capable of covering the wide range of flight conditions encountered in practical operation. In addition, the flight of insects and birds which involves complex flapping motions do not follow the classical aerodynamics based quasi-steady mechanisms of lift generation without taking into account of the flow characteristics surrounding the flapping wing (Shyy et al., 2009; Trizila et al., 2011; Shyy et al., 1999; Sane, 2003; Alexander, 2002; Dickinson et al., 1999; Arora et al., 2014). Developing a better understanding of this process which addresses the issues of scaling and energy optimization (Kang et al., 2011; Kang and Shyy, 2013, 2014; Lee et al., 2015; Quinn et al., 2013) is expected to assist in simplified MAV design.

The phenomenon of thrust generation in birds was first reported by Knoller (1909) and Betz (1912), and hence is known as the *Knoller–Betz effect.* By considering a vertically heaving airfoil as a representation of bird wings, they stated that due to the plunging motion of wing an effective angle of attack was created which provided a force component in the horizontal direction and was responsible for thrust production, which was later experimentally proved by Katzmayr (1922). Many experimental and computational studies on rigid wing performing pure plunging motion (some studies also included active pitching) were conducted which supported the above argument (Freymuth, 1988, 1990; Triantafyllou et al., 1991; Lai and Platzer, 2000; Jones et al., 1998; Anderson et al., 1998; Lewin and Haj-Hariri, 2003). In all these studies either the wing flapped at a fixed position with an oncoming flow or the wing cruised through the flow whose speed could be controlled independently. Taking it further, the present study is conducted on a rigid self-propelled heaving airfoil (the forward translation is produced only due to flapping motion and both of them are interdependent or coupled) to mimic the operation of a biological flyer.

Some of the key findings of previous studies on an auto-propelled wing (Vandenberghe et al., 2004; Vandenberghe et al., 2006; Alben and Shelley, 2005; Lu and Liao, 2006; Zhang et al., 2009; Benkherouf et al., 2011; Hu and Xiao, 2014) are summarized here. Vandenberghe et al. (2004, 2006) experimentally revealed the presence of a stability limit beyond which a pure oscillating rectangular plate mounted on an axle can rotate in the transverse direction, indicating the onset of the generation of thrust. Alben and Shelley (2005), using an elliptical wing, numerically investigated the earlier (Vandenberghe et al., 2004) experiment and showed that beyond a critical Reynolds number (based on flapping frequency), unidirectional locomotion can be achieved for an initially non-locomoting body. Lu and Liao (2006) quantified the critical Reynolds number by varying the amplitude of an elliptical membrane and studied the dynamical behavior of the foil with different density ratios, and classified it as (a) steady, or (b) oscillatory movement. Zhang et al. (2009) studied the effect of varying the chord-thickness ratio (CR) for an elliptical and rectangular flapping foil between 1 and 100 on the symmetry breaking bifurcation. Hu and Xiao (2014) examined the propulsive performance of a three-dimensional plunging elliptical airfoil by varying the density and aspect ratio (defined as the span to chord ratio) and showed that the translational velocity and thrust coefficient increase with an increase in the aspect ratio.

These earlier studies demarcate the zones of stability/instability and quantify the critical plunging frequency or flapping Reynolds number beyond which pure plunging motion leads to thrust generation, as a function of amplitude, density and chord-thickness ratio. Furthermore, power requirements and efficiency for propulsion of a self-propelled airfoil due to interplay of flapping Reynolds number Re_f, plunging amplitude β and wing-fluid density ratio ρ^* need to be addressed. We aim to present a quantitative assessment of such issues for the zone in which propulsion is attained, develop their reduced-order models and highlight the relative impact of the governing parameters for a thin, rigid and plunging flat plate. Hence, the following are the key objectives of this work:

1. investigate the impact of flapping Reynolds number Re_f, plunging amplitude β and density ratio ρ^* on the propulsion velocity and energy requirements of a rigid-flat plate,
2. highlight the dominant flow structures that capture and explain the dynamics of thrust generation in a self-propelled plunging plate, and
3. formulate reduced-order models through surrogate modelling to establish a relationship between performance (power and efficiency) and system parameters (Re_f, ρ^* and β). Thereafter, identify the optimum operating conditions in forward flight including any tradeoff between these two performance parameters.

To the best of our knowledge, impact assessment of the chosen variables on propulsive performance of a plunging wing with the help of reduced-order models has not been pursued so far.

2. Problem description

2.1. Plunging kinematics and parameters

We consider an auto-propelled heaving rigid flat plate, unconstrained to translate in the horizontal direction, whereas plunging takes place in the vertical direction. The following parameters which are expected to play a vital role in propulsion are introduced to conduct a parametric study on the plunging airfoil. Chord C has been chosen as the length scale and flapping duration T (where $T = 1/\gamma$ and γ is the plunging frequency) as time scale for non-dimensionalizing them.

The dimensionless vertical displacement of the flat plate is given as

$$y(t^*) = -\beta \cos(2\pi t^*) \tag{1}$$

where $t^* = \gamma t$ and $\beta = A/C$ is the dimensionless plunging amplitude.

The flapping Reynolds number based on frequency is defined as

$$\mathrm{Re}_f = \frac{A\gamma C}{\upsilon} \tag{2}$$

where υ is the kinematic viscosity.

Due to the fluid–airfoil interaction, a hydrodynamic force is exerted on the flat plate. The horizontal component of this force will be responsible for the forward locomotion along the x-axis. The dimensionless horizontal position of the plate x_p^* is updated by the following equation

$$\frac{d^2x_p^*}{dt^{*2}} = \frac{2\pi^2\beta^2}{\rho^*\delta}\langle F_x\rangle \tag{3}$$

In Eq. (3), $\langle F_x\rangle$ is the thrust coefficient defined as

$$\langle F_x\rangle = \frac{\bar{F}_x}{\frac{1}{2}\rho_f V^2 C} \tag{4}$$

where $V = 2\pi A\gamma$ is the maximum plunging velocity, $\bar{F}_x$ is the instantaneous thrust calculated using momentum exchange method and is explained in Section IIIA.2.

ρ^* is the density ratio defined as

$$\rho^* = \frac{\rho_s}{\rho_f} \tag{5}$$

where ρ_s and ρ_f are the densities of the plate and fluid, respectively. δ is the thickness to chord ratio which been fixed at 2% in this work and is very close to that of a real insect wing (Shyy et al., 2008, 2010). Zhang et al. (2009) in their study showed that for $\delta \leq 2\%$, rectangular foils propelled faster than elliptic ones. Hence, all analysis has been conducted assuming a rectangular cross-sectional shape of the wing.

The dimensionless velocity component in the horizontal direction U, is updated by the following rule

$$U = \frac{u}{V} = \frac{1}{2\pi\beta}\frac{dx_p^*}{dt^*} \tag{6}$$

where u is the dimensional instantaneous translational velocity. The translational Reynolds number is defined as

$$\mathrm{Re}_u = \frac{\bar{u}\,C}{\upsilon} \tag{7}$$

where $\bar{u}$ is the time-averaged translational velocity attained by the plate at cruising condition.

Another important dimensionless number related to the flapping flight indicative of the vortex shedding is the Strouhal number which is defined as

$$St = \frac{\gamma A_w}{\bar{u}} \tag{8}$$

where A_w is the width of the wake and is taken as 2 A (twice the plunging amplitude) (Lu and Liao, 2006). Strouhal number can also be expressed as $St = 2\mathrm{Re}_f/\mathrm{Re}_u$ and it represents the ratio of plunging acceleration forces to the pressure or thrust/drag forces generated due to flapping. In terms of time scales, it is a comparison of the time taken to horizontally traverse characteristic length (chord C in present study) with the plunging time period (Benkherouf et al., 2011).

Table 1 shows the parameter range, type of model and shape of wing considered in the earlier studies on self-propelled rigid plunging wing along with their key contributions. Although significant findings for identification of critical parameters governing propulsion were reported, none of these studies covered aspects related to flow patterns and the collective impact of these parameters on efficiency and input power at cruising conditions. Moreover, these analyses have inherently employed thick plates or elliptical membranes, and a density ratio that may not be compatible with the morphological parameters of biological flyers.

To obtain an exhaustive understanding of the dynamics associated with the parameters of interest, the selection of the range of design variables encompassing these earlier studies was deemed necessary. Hence, a range of parameters which is also in agreement with that of smallest insect flight (such as *Encarsia Formosa* and *Drosophila melanogaster*) (Shyy et al., 2008, 2010) and as shown in Table 2 has been chosen. Moreover, it has earlier been shown that for low ρ^*, high β and $\mathrm{Re}_f \leq 10$, an instability leading to translation does not result in a steady propulsive velocity (Alben and Shelley, 2005). Since the focus of this work is on efficiency and power quantification for steady flight (or cruising condition), thus, the lower limit for Re_f was chosen to be Re_f=20. It should also be noted that the wing or tail of flying and swimming animals has a density

Table 1
Highlights of earlier studies on self-propelled rigid plunging membrane.

Reference	Model/Shape	Parameter Range	Merits
Alben and Shelley (2005)	2-D numerical, Elliptical membrane	$\beta = 0.5$ $\delta = 5–30.3\%$ $\rho^* = 1–100$ $Re_f = 1–50$	(a) First simulation of a rigid self-propelled wing (b) Determined critical Re as a function of ρ^*
Vandenberghe et al. (2004), Vandenberghe et al. (2006)	Experimental Flat plate	$\beta = 0.2–0.65$ $\delta = 8.4 – 16.8\%$ $\rho^* = 7.2$ $Re_f = 1–1500$	(a) Originated the novel idea of a self-propelled wing
Lu and Liao (2006)	2-D numerical Elliptical membrane	$\beta = 0.2–1$ $\delta = 8.3\%$ $\rho^* = 1–100$ $Re_f = 1–100$	(a) Determined critical Re as a function of β
Zhang et al. (2009)	2-D numerical Flat plate & Elliptical membrane	$\beta = 0.4$ $\delta = 1–100\%$ $\rho^* = 4$ $Re_f = 31.84$	(a) First study to consider wing shape and thickness effects (b) Determined critical Re as a function of δ
Hu and Xiao (2014)	3-D numerical Elliptical membrane	$\beta = 0.5$ $\delta = 10\%$ $\rho^* = 4–32$ $Re_f = 20 – 80$	(a) First study to consider three-dimensional effects

Table 2
The range of parameters (or design space) considered in this work for surrogate modelling.

Design Variable	Minimum value	Maximum value
ρ^*	10	100
Re_f	20	100
β	0.2	1

ratio ρ^*~10^1 – 10^3 (Lu and Liao, 2006). In this work ρ^* has been considered to lie within 10^1 – 10^2 in order to avoid issues related to convergence of numerical solution in larger density ratio scenarios.

The cycle-averaged input power P_i^* is given as

$$P_i^* = \frac{1}{T}\int_t^{t+T} \left|F_y\, v\right| dt \tag{9}$$

Here F_y is the instantaneous vertical force acting on the plunging wing and T is the time duration of one cycle. For the sake of comparison, the input power can be non-dimensionalized to obtain the power coefficient P_i as

$$P_i = \frac{P_i^*}{\frac{1}{2}\rho_f V^3 C} \tag{10}$$

In self-propelled studies, the net horizontal force is zero at the cruising condition (thrust balances the drag) and hence, the output power cannot be calculated in a fashion similar to the input power (Schultz and Webb, 2002). Instead of power, the averaged kinetic energy per cycle due to forward motion, which represents the output work, is calculated (Kern and Koumoutsakos, 2006) and is given by

$$E = \frac{1}{T}\int_t^{t+T} \frac{1}{2} m u^2 dt \tag{11}$$

The propulsive efficiency η is a measure of the performance of the forward locomotion obtained by the plunging plate and is calculated as

$$\eta = \frac{E}{W} \tag{12}$$

where W is the input work per cycle given by

$$W = P_i^*.\ T \tag{13}$$

3. Methodology

The present study encompasses two stages of numerical modelling: (a) Fluid solver, for deciphering the fluid flow around plunging wing and force calculation due to fluid-structure interaction, and (b) Surrogate modelling, for formulating a relationship between the objective functions (i.e. efficiency and power) and design parameters (i.e. Re_f, ρ^* and β). The description of these approaches is given in the following sections.

3.1. Fluid solver

The lattice Boltzmann method (LBM) which involves the solution of discretized Boltzmann equation for the particle distribution function (Ladd, 1994; Succi, 2001; Chen and Doolen, 1998), has been used for performing the numerical simulations. The most popular amongst the LB methods is the Bhatnagar, Gross and Krook (BGK) or the single-relaxation-time (SRT) model. However, SRT exhibits numerical instability at high Re (low values of relaxation time) and displays spurious oscillations in force measurement (Arora et al., 2016). Sighting these disadvantages which posed an impediment in solving the fluid flow, the authors moved on to the multi-relaxation-time (MRT) model that successfully overcame the problems faced and has thus been employed in the present study. A brief description of this method in given in the Appendix and calculation of macroscopic variables (flow field around the wing, i.e. $\boldsymbol{u}$, $\boldsymbol{v}$ and p) from the distribution functions is provided in our earlier publication (Arora et al., 2014). The moving boundary condition and force calculation are reiterated here.

3.1.1. Treatment of moving boundary

For the case of a moving boundary, the solid surface is represented by a set of boundary nodes which lie at the mid points of the links connecting the fluid and solid nodes. With reference to Fig. 5 in Arora et al. (2014), the distribution functions reflected back from the solid into the fluid nodes can be written as

$$f_{\bar{\alpha}}(\mathbf{x}_f,\ t+1) = f_{\alpha}(\mathbf{x}_s,\ t) + 2w_{\alpha}\rho\frac{3}{c^2}\mathbf{e}_{\bar{\alpha}}.\ \mathbf{u}_b \tag{14}$$

The last term in Eq. (14) accounts for the momentum transfer between the fluid and moving solid boundary (Ladd, 1994). Here $\mathbf{e}_{\bar{\alpha}} = -\mathbf{e}_{\alpha}$ and $\mathbf{u}_b$ is the velocity of the boundary node, assumed to be located exactly halfway along the link between solid and fluid nodes, and is given by

$$\mathbf{u}_b = \mathbf{U} + \boldsymbol{\omega} \times \left(\mathbf{x} + \frac{1}{2}\mathbf{e}_{\alpha} - \mathbf{X}\right) \tag{15}$$

where $\mathbf{U}$ is the translational velocity, $\boldsymbol{\omega}$ is the angular velocity and $\mathbf{X}$ is the position vector of the center of mass of the solid.

In this method, the lattice nodes on either side of the boundary surface are treated in an identical fashion, i.e., the fluid fills the entire domain (Ladd, 1994). With this modification, at each boundary node the two incoming distributions $\tilde{f}_{\alpha}(\mathbf{x},\ t)$ and $\tilde{f}_{\bar{\alpha}}(\mathbf{x}+\mathbf{e}_{\alpha},\ t)$ from the fluid and the solid sides, respectively, corresponding to velocities $\mathbf{e}_{\alpha}$ and $\mathbf{e}_{\bar{\alpha}}$ along the link connecting $\mathbf{x}$ and $\mathbf{x}+\mathbf{e}_{\alpha}$, are updated according to,

$$f_{\alpha}(\mathbf{x}+\mathbf{e}_{\alpha},\ t+1) = \tilde{f}_{\bar{\alpha}}(\mathbf{x}+\mathbf{e}_{\alpha},\ t) + 2w_{\alpha}\rho\frac{3}{c^2}\mathbf{e}_{\alpha}.\ \mathbf{u}_b \tag{16}$$

$$f_{\bar{\alpha}}(\mathbf{x},\ t+1) = \tilde{f}_{\alpha}(\mathbf{x},\ t) - 2w_{\alpha}\rho\frac{3}{c^2}\mathbf{e}_{\alpha}.\ \mathbf{u}_b \tag{17}$$

This approach ensures that mass is conserved at the boundary nodes and also avoids the necessity of creating and destroying fluid as the solid particle moves (covering/uncovering of the fluid/solid nodes).

3.1.2. Force calculation

Due to the boundary node interactions, a force is exerted on the solid which is given by

$$\mathbf{F}\left(\mathbf{x}+\frac{1}{2}\mathbf{e}_{\alpha},\ t+\frac{1}{2}\right) = 2\left[\tilde{f}_{\alpha}(\mathbf{x},\ t) - \tilde{f}_{\bar{\alpha}}(\mathbf{x}+\mathbf{e}_{\alpha},\ t) - 2w_{\alpha}\rho\frac{3}{c^2}\mathbf{e}_{\alpha}.\ \mathbf{u}_b\right]\mathbf{e}_{\alpha} \tag{18}$$

The total force $\bar{\mathbf{F}}$ on the solid object is obtained by summing $\mathbf{F}$ over all the nodes that constitute the boundary of the object along the directions α which involve the exchange of distributions from fluid to solid nodes or vice-versa,

$$\bar{\mathbf{F}}\left(t+\frac{1}{2}\right) = \sum_{all\ x_b}\sum_{\alpha}\mathbf{F}\left(\mathbf{x}+\frac{1}{2}\mathbf{e}_{\alpha},\ t+\frac{1}{2}\right) \tag{19}$$

The overall force is calculated at the intermediate integer time step by taking the average of the total forces at half integer

time steps,

$$\bar{\mathbf{F}}(t) = \frac{1}{2}\left[\bar{\mathbf{F}}\left(t-\frac{1}{2}\right) + \bar{\mathbf{F}}\left(t+\frac{1}{2}\right)\right] \tag{20}$$

Issues pertaining to the accuracy of force measurement can be resolved by improving the resolution of the moving body by refining the mesh near the surface of the solid to capture the minutest of details. However, refinement of the grid throughout the domain (even in those regions where the flow is not expected to evolve rapidly) is computationally expensive and inefficient. Thus, the present study employs a novel and an unconventional shifting discontinuous-grid-block LBM where a fine block translates with the moving solid on a carpet of coarse block (Arora et al., 2016). In this method, the fine block shifts by $m\,\Delta x_f$ (where $m = \Delta x_c/\Delta x_f$ is the grid refinement ratio and Δx_f is the lattice spacing in fine block) along the X or Y direction as the solid (wing) traverses a unit lattice in coarse block i.e. Δx_c. Hence, at the end of a unit time step in coarse grid, the distance propagated by the object in fine grid is examined. If it exceedsΔx_c, a layer of fine grid is added (removed) along (against) the direction of translation.

3.1.3. Computational domain

A pictorial representation of the computational domain is shown in Fig. 1. As shown, a dynamic multi-block (finer mesh) has been considered around the structure in an overall domain of size 50C × 20C in coarse lattice units. The leading edge of wing was positioned 20C downstream of the inlet and 30C upstream of the outlet. No slip boundary condition (zero fluid velocity) was applied on the top and bottom walls of the domain along with the inlet. At the outlet, fully developed boundary condition (zero normal derivative of velocity i.e. $\partial u/\partial x = 0$) was imposed. Similar to the fine-block, the entire computational domain shifted with the movement of the wing. Therefore, as the wing translated a unit distance in the coarse block, a layer of fluid nodes was removed from outlet and added at the inlet. When adding new layers, the post collision distribution functions at the existing inlet boundary were replicated onto the newly added layer. This ensured that far upstream the pressure gradient was zero i.e. $\partial p/\partial x = 0$. Hence, with this technique a finite domain can be epitomized as an infinite region.

To benefit from the use of LBM, the code developed was parallelized using MPI (Message Passing Interface) in which the domain along the x direction is sliced into $\boldsymbol{n}$ sub-zones, where $\mathbf{n}$ is the number of processors. Thus, each processor is assigned a sub-domain with (50/$\boldsymbol{n}$)C x 20C physical size.

3.1.4. Convergence and validation

To test for the mesh independence and convergence of the numerical method, three cases with progressively improved mesh resolutions were examined. In case 1, a uniform coarse grid without any local refinement was considered. Whereas in

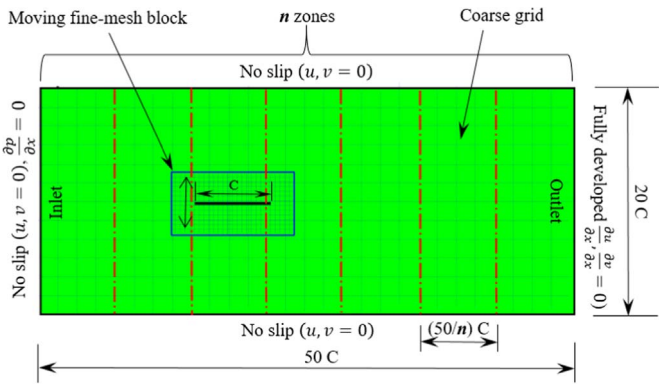

Fig. 1. Layout of the computational domain with imposed boundary conditions segregated into different zones (by red lines) handled by multi-processors. A recently developed discontinuous-grid-block LBM is implemented where a fine block translates with the moving solid on a carpet of coarse block (Arora et al., 2016).(For interpretation of the references to color in this figure,the reader is referred to the web version of this article.)

Table 3
Mesh resolution for different cases shown in Fig. 3.

Description		Grid Spacing
Uniform coarse grid	Case 1	$\Delta x = 0.01C$
Uniform coarse grid with local refinement (moving fine block)	Case 2	$\Delta x_f = 0.005C$, $\Delta x_c = 0.01C$
	Case 3	$\Delta x_f = 0.0025C$, $\Delta x_c = 0.005C$

case 2 and case 3, a fine mesh was taken around the wing (with grid refinement ratio $m=2$). The description of the grid spacing for these cases is given in Table 3. The dimensions of the dynamic fine mesh block which moved along with the wing was taken as $2C \times 3C$ to ensure that the plunging plate was well confined within the boundaries of the fine block. The convergence test for the size of moving mesh was also performed and it was observed that the horizontal velocity profile with the current dimensions of moving fine mesh exhibited good agreement with the stationary fine mesh that spanned the entire horizontal length of the computational domain (i.e., $50C \times 3C$).

Fig. 2 shows a schematic diagram of the orientation of the thrust and drag force associated with the vertical plunging motion considered in this study. Since drag always opposes the imposed motion, it acts along the vertical direction and the thrust (analogous to lift) responsible for propulsion acts horizontally.

A comparison of the dimensionless thrust $<F_x>$ and drag $<F_y>$ with time between these cases is shown in Fig. 3. As evident, there is not much deviation in the forces and the degree of quantitative agreement with case 3 improves from case 1 to case 2. However, to strike a balance between accuracy associated with mesh resolution and computational expenses, grid parameters corresponding to case 2 were chosen for performing all numerical simulations.

A moving average method, that resulted in change in average force coefficients by $< 10^{-3}\%$, has been used to reduce fluctuations and smoothen the force history over the entire simulation period (Arora et al., 2014). One of the reasons that directly contributes to these fluctuations was the fact that in halfway bounceback LBM, certain grid points undergo transitions from non-fluid region to fluid region or vice versa due to movement of the solid. Thus, the number of fluid nodes is not conserved and the volume occupied by the solid object varies which contributes to the noise. A few earlier studies have also reported such oscillations in their force measurements pertaining to the moving boundary using LBM (Arora et al., 2016, Aono et al., 2010; Lallemand and Luo, 2003.).

In order to validate the solver, simulations for a symmetric elliptical airfoil at different flapping Reynolds numbers were conducted and the corresponding translational Reynolds number Re_u was compared against the numerical results of Alben

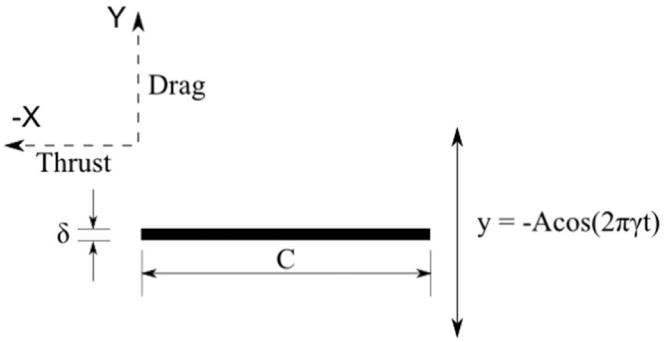

Fig. 2. A schematic representation of the plunging wing with direction of thrust and drag forces.

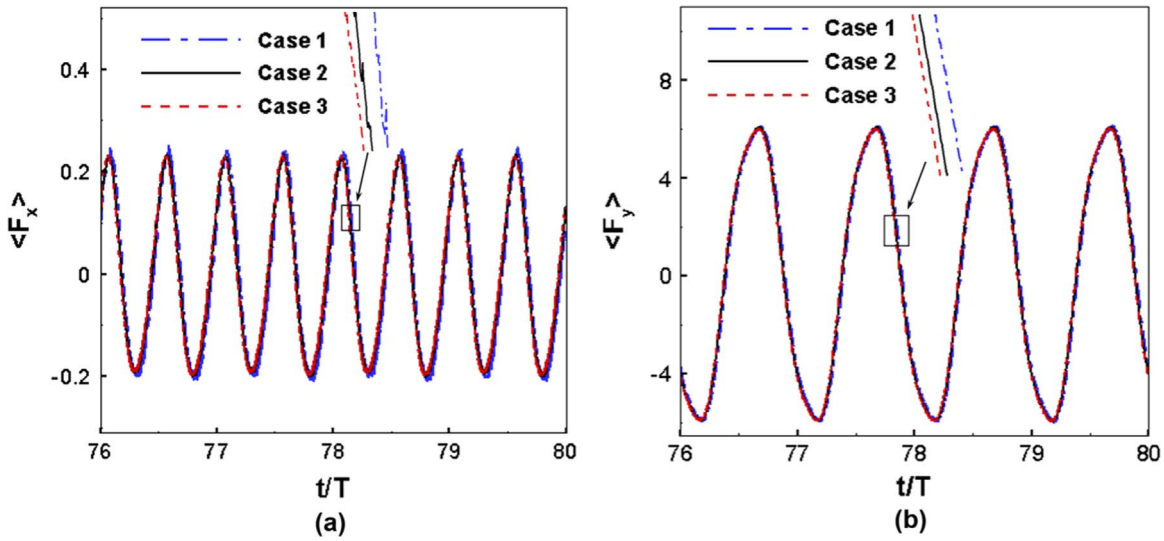

Fig. 3. A comparison in (a) thrust and (b) drag coefficients with different grid spacing at $Re_f = 20$, $\beta = 0.4$ and $\rho^* = 55$. The description of mesh resolution for these cases is given in Table 3. The inset shows zoomed version of rectangular snapshot.

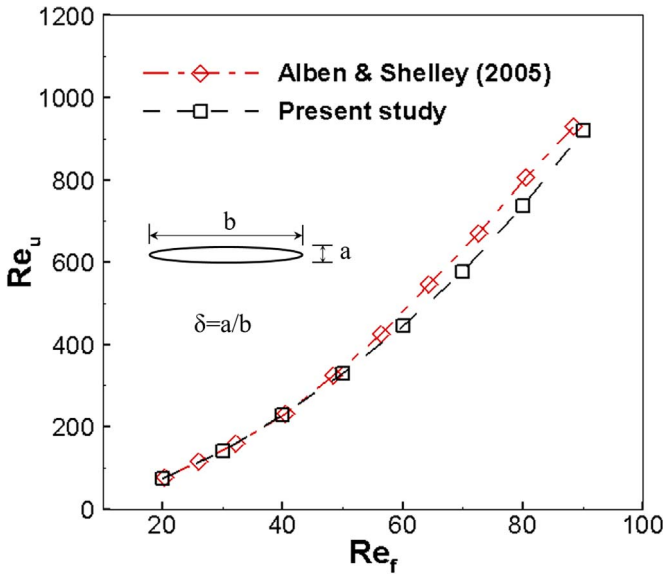

Fig. 4. A comparison of translational Reynolds number Re_u as a function of flapping Reynolds number Re_f between present study and Alben and Shelley (2005) for an elliptical airfoil with $\rho^* = 32$, $\beta = 0.5$ and $\delta = 0.1$.

and Shelley (2005). The ratio of amplitude to chord β and mass density ratio ρ^* was taken as 0.5 and 32, respectively as was considered in their work (Alben and Shelley, 2005). The thickness to chord of the elliptical membrane, δ, was kept constant as 0.1. The translational Reynolds number Re_u in the present study was calculated by time-averaging the horizontal velocity over 10 plunging cycles after forward flight was achieved. As is shown in Fig. 4, the results obtained show good qualitative and quantitative agreement and were used to validate the numerical model.

3.2. Surrogate modelling

Surrogate modelling involves construction of a continuous function (or surrogate) of a set of independent 'design' variables from a limited amount of data that could have been obtained from pre-computed high fidelity simulations or physical measurements. It helps in systematically organizing data to ascertain the interplay between different variables. This reduced-order model also offers a global outlook and assists in determining the influence on the dependent variables which otherwise may not be ascertainable by individually varying each design variable. The surrogates provide fast evaluations of the various modelling and design scenarios, thereby making sensitivity and optimization studies feasible (Quiepo et al., 2005; Goel et al., 2008; Shyy et al., 2001; Shyy et al., 2011).

3.2.1. Design space

Surrogate modelling begins by identifying the range (minimum and maximum values) in which the 'design' or independent variables are to be studied. This process is known as setting up of the design space. Thereafter, a number of locations in this design space are chosen systematically where numerical simulations or physical experiments will be conducted. The set of locations comprise what is known as the Design of Experiments (DOE). The two commonly used procedures for the creation of DOE are Face Centred Cubic Design (FCCD) and Latin Hypercubic Sampling (LHS). FCCD provides a total of 2^N+2N+1 sampling points in a normalized design space: 2^N corner points, $2N$ face-centred points and 1 body-centred point (Goel et al., 2008), where N is the number of design variables. LHS generates sampling points by maximizing the minimum distance between them and is usually employed after FCCD to obtain additional test points or to fill in the remainder of design space.

3.2.2. Surrogate models

Once data is obtained at the selected 'training' points of DOE, it is used for framing the surrogate model and carrying out a sensitivity analysis. Surrogate models can be categorized in two groups, namely parametric (e.g., Polynomial Response Surface (PRS), Kriging) and non-parametric (e.g., Neural Networks) (Quiepo et al., 2005). The surrogates constructed in this study are based on the PRS and Kriging approach. In polynomial response surface, the function of interest g is approximated as a linear combination of polynomial functions of design variables $\mathbf{y}$ (Quiepo et al., 2005; Goel et al., 2008; Shyy et al., 2001).

$$g(\mathbf{y}) = \sum_i h_i a_i(\mathbf{y}) + \varepsilon \tag{21}$$

Here h_i is estimated through a least-squares method so as to minimize the variance, $a_i(\mathbf{y})$ are basis functions, i is the

number of terms which depend on the degree of PRS chosen and the errors ε have an expected value (i.e., $\langle\varepsilon\rangle$) equal to zero. The adjusted coefficient of multiple determination ($R_{adj}{}^2$) computes the prediction capability of the polynomial response surface approximation (Shyy et al., 2011) which is defined as

$$R_{adj}^2 = 1 - \frac{\sigma_a^2(N_s - 1)}{\sum_{i=1}^{N_s}(y_i - \bar{y})^2} \tag{22}$$

where N_s is the number of sample or training points, y_i is the true or actual value of the objective function, σ_a is the RMS error of the polynomial fit at the training points and $\bar{y}$ is the mean value of the objective function. A good polynomial fit should have an $R_{adj}{}^2$ value close to 1.

Another parameter called as 'Prediction Error Sum of Squares' (PRESS) is very commonly used as a measure of the accuracy of the constructed surrogate model and quantifying the error (Quiepo et al., 2005; Goel et al., 2008). The root mean square PRESS is calculated as

$$PRESS_{RMS} = \sqrt{\frac{1}{N_s}\sum_{i=1}^{N_s}\left(y_i - \hat{y}_i^{(-i)}\right)^2} \tag{23}$$

where y_i is the true value at sample point $\mathbf{x}^{(i)}$ and $\hat{y}_i^{(-i)}$ is the estimated value using a surrogate model constructed by considering all the sample points except the source point ($\mathbf{x}^{(i)}$,y_i), also known as the 'leave-one-out' strategy.

The Kriging model estimates the objective function g as a sum of two terms: (a) linear polynomial expression and (b) systematic departure Z (Quiepo et al., 2005; Goel et al., 2008).

$$g(y) = \sum_j h_j a_j(y) \; + \; Z(y) \tag{24}$$

$Z(y)$ symbolizes frequency variations around the model which is correlated on the basis of distance between the sampling points. The most popular correlation methods for evaluation of $Z(y)$ are Gaussian, linear, exponential, cubic and spline functions.

3.2.3. Sensitivity analysis

Using the constructed surrogate model, sensitivity analysis can be performed to examine the influence of design parameters and can be useful in assessing their hierarchical order of importance on the overall objective function (Goel et al., 2008). It also helps in measuring the extent of cross-interaction and interlinked influence of the design variables on the objective function. In the present study, a method based on the contribution of the design variables to the variance of the objective function has been implemented (Quiepo et al., 2005). There are two sensitivity indices, namely (a) main, and (b) total sensitivity. The former is a measure of the effect of individual parameters on the change in output, whereas the latter indicates the combined or collective impact of the design variables in the output variation.

4. Results and discussion

In this section, results obtained for various Re_f, ρ^* and β through numerical simulation of a plunging thin two-dimensional rectangular flat plate which can freely propel in a quiescent fluid will be presented and discussed. To induce instability, an initial momentum corresponding to 1% of the maximum plunging velocity (in the -X-direction) was imparted to the flat plate for the first half plunging cycle in all cases. Here instability is defined as the state when a small perturbation (in our case, a small momentum) grows causing the plunging wing (unconstrained horizontally) to propel in the direction of imparted momentum. However, the magnitude of the small momentum was found to not affect the final velocity at cruising condition other than to ensure that the wing moved towards the domain inlet (or towards left).

4.1. Hovering

While the main focus of this work is on propulsion during forward flight, it is of interest to examine a hovering scenario when no propulsive force is generated. As shown in Fig. 5, we consider a case for Re_f=1, ρ^*=55 and β=0.6 in which no propulsion was obtained. The simulation was run till 50 plunging cycles were completed with no instability being registered, i.e., no horizontal locomotion was achieved and the wing only heaved up and down about a fixed mean position. In Fig. 5(a), the upstroke begins, vortices form at both the edges and grow till the midstroke (shown in Fig. 5(b)). As the wing reaches the upper extreme position and starts the downstroke, both leading and trailing edge vortices are dissipated and new opposite pair of vortices are formed (Fig. 5(c)). The vortices experience relatively large viscous dissipation by the end of the stroke without being shed. As a result, there is no wing-wake interaction and consequently asymmetry which could have driven the wing into forward motion is not realized. A similar formation and dissipation of vortices occurred during the downstroke with the initial perturbation in the form of a small momentum failed to grow even after the plate completed the aforementioned plunging strokes.

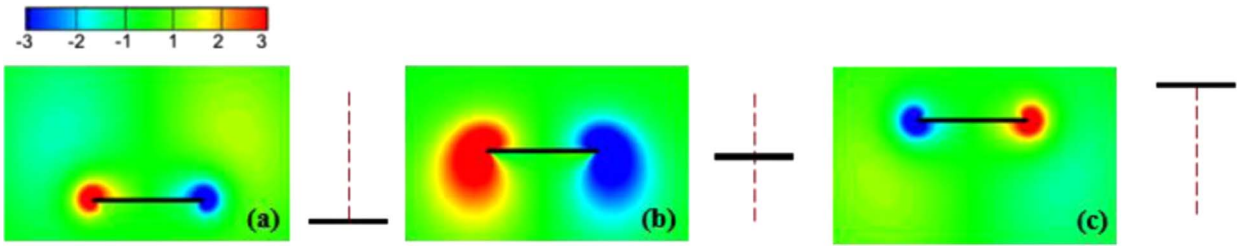

Fig. 5. The non-dimensionalized vorticity contours used to illustrate the flow field around a flat plate at cruising condition plunging at $Re_f=1$ with $\rho^*=55$ and $\beta=0.6$. Vorticity scale chosen for non-dimensionalization is $\omega_c = 2\pi\beta\gamma$. The corresponding right image shows the instantaneous positions and the trajectory during one cycle. Red and blue colors indicate anti-clockwise (out of the plane of pater) and clockwise rotation (into the plane of paper), respectively. An animation depicting the vortex evolution is provided as supplementary material (Movie 1).(For interpretation of the references to color in this figure,the reader is referred to the web version of this article.)

Supplementary material related to this article can be found online at http://dx.doi.org/10.1016/j.jfluidstructs.2016.08.005.

4.2. Forward flight

By examining the vorticity flow structures, we describe the dynamics that emanates from the plunging motion that imparts a forward thrust and pushes the wing into cruising condition.

The temporal variation of the dimensionless horizontal velocity of the wing for $Re_f=55$, $\rho^*=55$ and $\beta=0.4$ is shown in Fig. 6. The points (**i**), (**ii**), (**iii**) and (**iv**) marked in this figure represent the time instants $t/T = 0.5$, 5.5, 10 and 40.5, respectively, at which the vorticity contours around the plate are plotted in the inset. As is evident, instability is achieved with the initial perturbation growing in the first few plunging cycles and the wing begins to propel towards the left. Subsequently, the velocity magnitude increases until it reaches the cruising condition at around the 20th cycle. Examination of the vorticity structures around the flat plate reveals negligibly small horizontal velocity in the early stages (i.e., (i)) as the vortical flow structures around the plate are near symmetrical. At (ii), the wing is shown interacting with the previously shed vortices which induces flow asymmetry resulting in thrust generation and initiation of propulsion. At (iii), the vortex attached to the trailing edge is seen interacting with an oppositely rotating vortex shed during the previous downstroke from the leading edge. This formation of a vortex dipole diminishes the strength of suction that would have existed when vortices of either rotation are present unaccompanied, like at the leading edge where low pressure is created due to an attached solo LEV. Consequently, these high and low pressure regions assist in imparting a force to the wing essential for propulsion. This phenomenon of wing wake interaction is, therefore, responsible for the growth of the initial momentum perturbation. At (iv), the wing is shown to have attained a cruising velocity with two opposite rotation vortices being shed per cycle, one during the upstroke and other during the downstroke. Both the half strokes are identical and mirror images of each other.

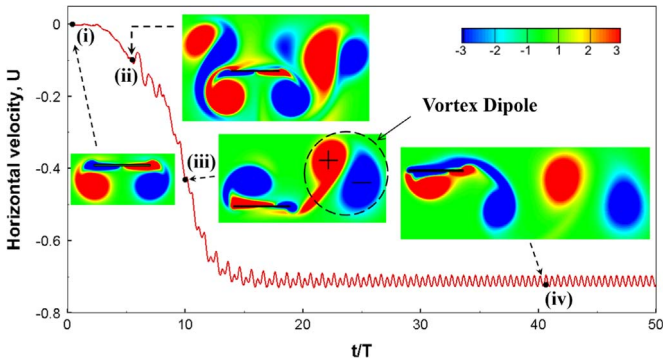

Fig. 6. Dimensionless horizontal velocity of the plunging airfoil at $Re_f = 20$, $\rho^*=55$ and $\beta=0.4$ as a function of number of cycles with $Re_u = 89.5$. Vorticity contours of fluid flow at (i) $t/T=0.5$, (ii) $t/T=5.5$, (iii) $t/T=10$ and (iv) $t/T=40.5$ are plotted in the inset. Red and blue colors indicate anti-clockwise (out of the plane of pater) and clockwise rotation (into the plane of paper), respectively. An animation illustrating the vortex evolution is provided as supplementary material (Movie 2).(For interpretation of the references to color in this figure,the reader is referred to the web version of this article.)

Supplementary material related to this article can be found online at http://dx.doi.org/10.1016/j.jfluidstructs.2016.08.005.

For this representative case of $Re_f=20$, $\beta=0.4$ and $\rho^*=55$, the transient thrust and drag coefficients (i.e, $<F_x>$ and $<F_y>$), normalized vertical velocity and normalized vertical displacement along with flow structures at cruising condition are shown in Fig. 7. The pressure distribution at the leading and trailing edges of the wing at maximum and minimum thrust

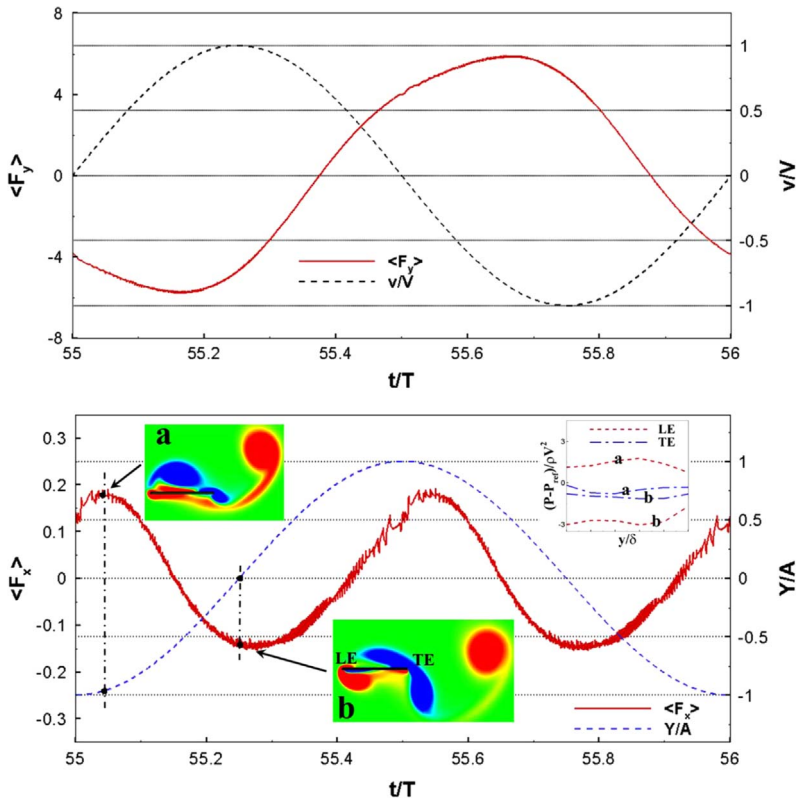

Fig. 7. Drag coefficient $< F_y >$ and non-dimensional vertical velocity (upper portion) and Thrust coefficient $< F_x >$ and non-dimensional vertical displacement (lower portion) at cruising condition for Re_f=20, β=0.4 and ρ^*=55. The wing is moving leftwards (-X direction). Flow structures around the wing are shown at different time instants and responsible for crests and troughs in thrust coefficient. The inset in upper right corner displays the pressure at leading and trailing edge at time instants (a) and (b). Situations (a) and (b) correspond to $P_{LE} > P_{TE}$ and $P_{LE} < P_{TE}$, respectively.

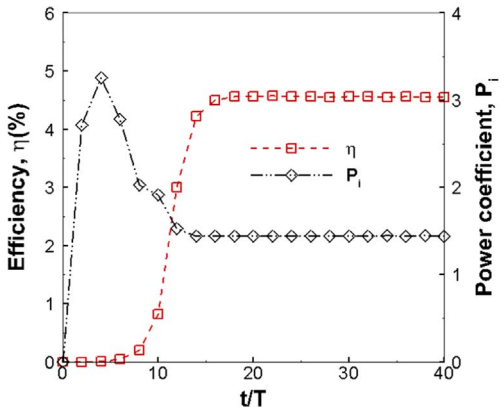

Fig. 8. Cycle-averaged propulsive efficiency η and input power coefficient P_i for Re_f =55 with ρ^*=55 and β=0.4.

coefficient is also shown in the inset. As can be observed, the pressure difference across the wing chord (i.e., $\Delta P = P_{LE} - P_{TE}$) changes from positive to negative as the wing undergoes upstroke (moving from lowermost (a) to mean position (b)). At position (a), a new LEV (red) is beginning to develop on the lower side of the plate and the LEV (blue) that formed on the upper side during downstroke is about to merge with the nascent TEV of same rotation. At position (b), the LEV on the lower side has grown and remains attached creating a zone of low pressure and the vortex near the trailing edge slips away, leading to $P_{LE} < P_{TE}$. At the end of the upstroke, flow structures similar to (a) were found to exist on the lower side of the plate and were again responsible for $P_{LE} > P_{TE}$. This reversal in pressure difference manifests in the form of time varying thrust that changes from positive (deceleration) to negative (acceleration) and prevails throughout the cruising condition and is responsible for the undulations registered in the velocity profile.

Fig. 8 shows the trend of cycle-averaged efficiency η and power coefficient P_i for the same case. In all simulations, a similar behavior is observable where the input power initially increases when there is a sudden loss in symmetry of the flow field and extra power is needed by the plate to overcome high drag. In addition, a thrust that is higher than that during cruising condition is required to move the plate and is also evident from the power curve. Within a few cycles after the onset of forward motion, the efficiency increases and reaches a maximum when cruising velocity is attained. It should be noted that the cruising condition efficiency $<\eta>$ and input power $<P_i>$ were determined by averaging over a time period $T_{ss} >> T$ after steady propulsion was achieved.

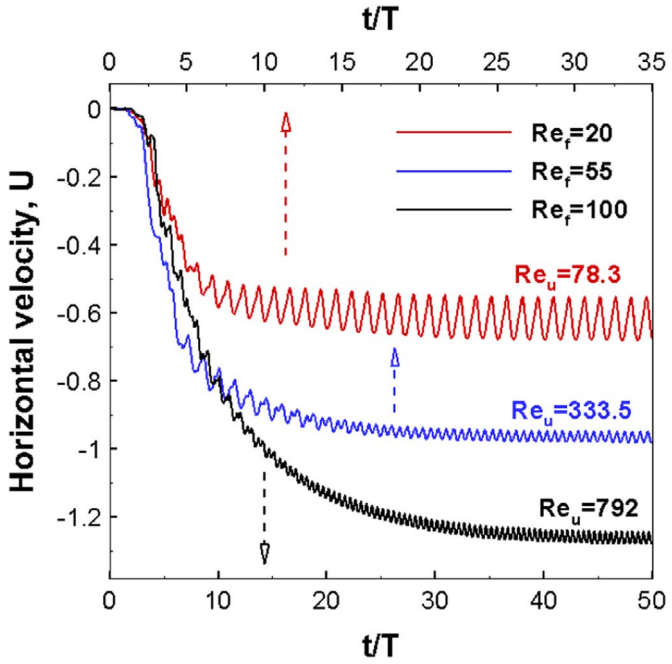

Fig. 9. Time variation of dimensionless propulsion velocity for the flat plate plunging for various Re_f with $\rho^*=55$ and $\beta=0.6$. The top and bottom horizontal axis represent the time scales for $Re_f=20$ and 55 and $Re_f=100$, respectively.

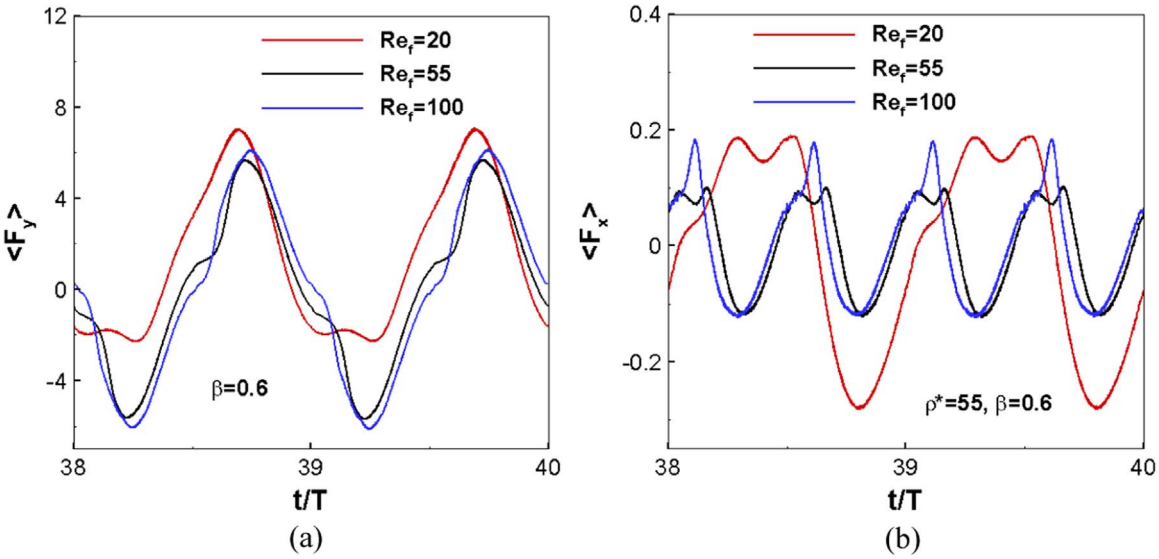

Fig. 10. Time variation of (a) drag and (b) thrust force coefficients for different Re_f with $\beta = 0.6$ and $\rho^* = 55$ at cruising conditions.

4.3. Parametric analysis

We now discuss the role of plunging parameters, i.e., flapping Reynolds number Re_f and plunging amplitude β, and the plate-fluid density ratio ρ^* on the cruising condition and highlight their impact on power requirement $< P_i >$ and propulsion efficiency $< \eta >$. Finally, their global implications are discussed through the developed 3rd degree polynomial response surfaces.

4.3.1. Effect of flapping Reynolds number (Re_f)

Fig. 9 shows the evolution of horizontal velocity profiles due to the action of the plunging motion for Re_f=20, 55 and 100 (with ρ^*=55 and β=0.6). As shown in the figure, the magnitude of the non-dimensional cruising velocity at Re_f=100 is more than double than that at Re_f=20. Due to the fact that a higher Reynolds number implies lower viscous dissipation (resulting in the likelihood of a stronger wing-wake interaction), the quantitative influence of wing-wake interaction, both in terms of aiding or hindering, depends on the alignment of the plate with shed vortices (Arora et al., 2014) and will be discussed shortly. More importantly, a greater number of cycles are shown to be needed to reach a cruising condition as Re_f increases.

To illustrate the dependence of Re_f on input power and efficiency, the time-dependent drag and thrust force coefficients are shown in Fig. 10. From the figure it is clear that coefficients of drag and thrust for Re_f=20 show a behavior that is very different from that observable for Re_f=55 and 100. In the case of the drag coefficient for Re_f=20, the variation during $38 \le t/T \le 38.5$ (upstroke) does not mirror that during $38.5 \le t/T \le 39$ (downstroke). As a result, the power required for driving the

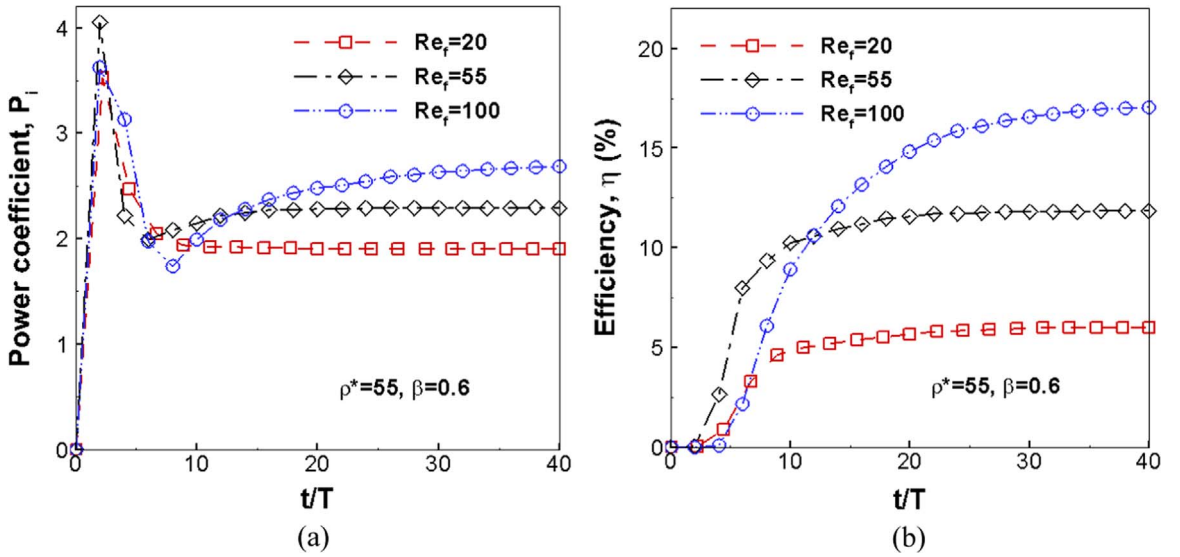

Fig. 11. The time-evolution of power coefficient P_i and efficiency η for various Re_f. The two parameters were calculated by averaging data at the end of each plunging cycle. Long after the initial transient period, the two parameters can be observed to have reached stagnation values indicating attainment of forward cruising flight. Further, for plunging motion at different Re_f, the input power and efficiency at cruising conditions are higher for situations with higher Re_f indicating the role of lower viscous dissipation on wing–wake interaction and reaching higher cruising velocities as shown in Fig. 9.

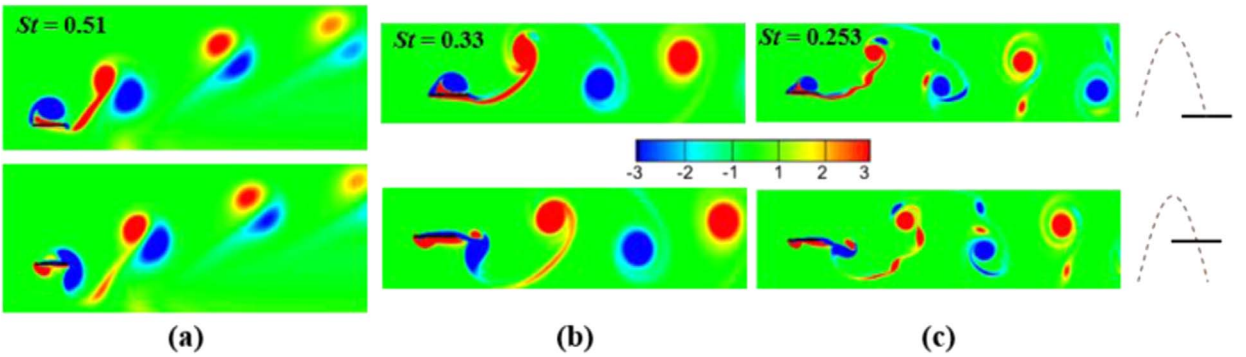

Fig. 12. Wake patterns at cruising condition for a flat plate plunging at Re_f of (a) 20, (b) 55 and (c) 100 with ρ^*=55 and β=0.6. The right-most column shows the instantaneous positions during the upstroke. Red and blue colors indicate anti-clockwise (out of the plane of paper) and clockwise rotation (into the plane of paper), respectively. (For interpretation of the references to color in this figure,the reader is referred to the web version of this article.)

heaving motion (as given by Eq. (9)) is lower for lower Re_f. A similar difference in profiles is also observed for thrust coefficient. The undulations in thrust coefficient decrease with increasing Re_f which explains the decreasing fluctuations in the horizontal velocity shown in Fig. 9. More importantly, the difference in thrust coefficient and interaction of plate with the shed vortex renders in the form of lower efficiency for low Re_f flows. To corroborate these arguments, the plunge cycle-averaged power coefficient and efficiency are plotted and shown in Fig. 11. This figure shows that long after the initial transient period when the effects of the impulsively moving plate have passed, the two parameters approach stagnation values indicating attainment of forward cruising flight. Further, the input power and efficiency at cruising conditions are higher for situations with higher Re_f indicating the role of lower viscous dissipation on wing–wake interaction and reaching higher cruising velocities as shown in Fig. 9.

A closer scrutiny of the flow patterns for the Re_f considered in earlier figures is presented in Fig. 12. The vortex patterns shown are at the beginning and half-way into the upstroke. For $Re_f = 20$, a wing-wake interaction is shown to occur during the upstroke at the trailing edge, wherein a deflected wake shed during the downstroke interacts with the plate leading to a suppression of pressure at the upper surface. This effect is found to be missing during the downstroke. For $Re_f = 55$ and 100, the wing-wake interaction was observable during both upstroke and downstroke with a symmetric vortex shedding pattern.

The wake patterns at cruising condition can also be characterized by Strouhal number (St). For the three cases discussed so far, $St = 0.51$, 0.33 and 0.253 for $Re_f = 20$, 55 and 100, respectively. It has earlier been found that (a) the thrust/pressure force dominates the plunging acceleration force when $St < 0.3$, (b) all these forces have equal importance and none of them can be ignored for $0.3 < St < 1.3$, and (c) the acceleration force becomes primarily significant with the pressure force being negligible for $St > 1.3$ (Benkherouf et al., 2011). In addition, viscous force plays a crucial role in the behavior of wake pattern which are determined by Re_f.

The interesting phenomenon of wake being slightly deflected from the line of propulsion occurs for $Re_f = 20$ ($St = 0.51$) as it lies in this transition zone. The transition zone demarcates the region of non-periodic and periodic propulsion velocity. This peculiar occurrence was probed further by examination of the net force exerted on the wing. It was found that the cycle averaged drag coefficient was not zero (also depicted in Fig. 10(a)), i.e., the fluid exerted an upward force and a net drag was generated. Since the plate was constrained to move in the vertical direction with a given kinematics, as a consequence the vortices were being shed at an upward angle with the horizontal. For $Re_f = 20$, the viscous forces were still strong and the vortices shed downstream disappeared quickly.

For $Re_f = 100$, on the other hand, a long trajectory of vortices is discernible in the wake. At this Reynolds number, the viscous forces are not strong enough which could shear the trailing edge vortex. Consequently the TEV remains attached to the trailing edge and as the wing translates at maximum propulsion velocity, it grows into an elongated tail. In addition, an oppositely rotating vortex reminiscent to the TEV was also shed along with it which later was annihilated. For $Re_f = 100$, a higher propulsive velocity was achieved with the wake patterns attained to be symmetric and with two oppositely directed vortices shed per cycle, one during the upstroke and other during the downstroke. At the onset of upstroke, the attached LEV above the plate (which was formed during the previous downstroke) was detached, advected downstream and

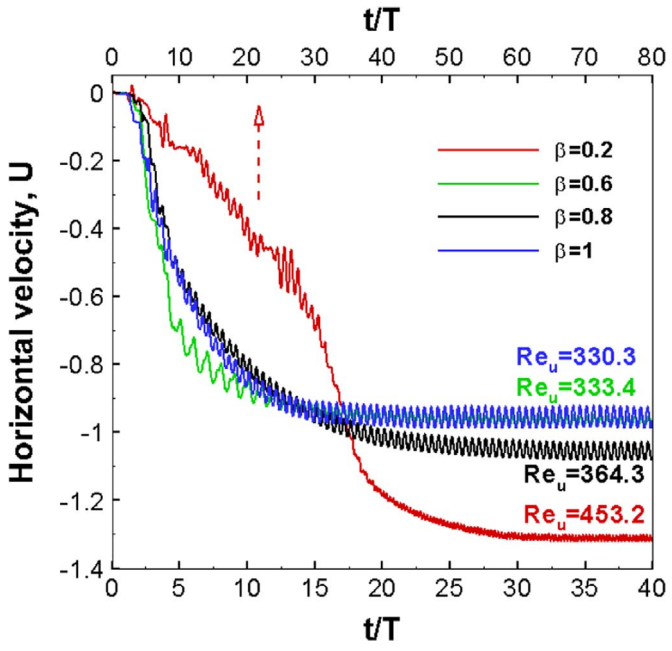

Fig. 13. Dimensionless propulsion velocity versus time for the flat plate plunging at $\beta = 0.2$, 0.6, 0.8 and 1 with $Re_f = 55$ and $\rho^* = 55$. The top and bottom horizontal axis represent the time scales for $\beta = 0.2$ and $\beta = 0.6$, 0.8 and 1, respectively.

coalesced with the TEV (about to form) of the same rotation, thereby strengthening the TEV. On the commencement of the downstroke, the TEV was shed and a similar shedding pattern was obtained.

4.3.2. Effect of plunging amplitude (β)

The effect of plunging amplitude β on propulsive velocity and propulsion performance is presented in this section. Fig. 13 shows a comparison of dimensionless velocity profiles obtained with β=0.2, 0.6, 0.8 and 1 at Re_f=55 and ρ^*=55. It can be observed that the magnitude of the propulsion velocity is highest for the lowest β. On increasing β, the cruising velocity decreased monotonically only for $0.2 \le \beta \le 0.6$ beyond which a moderate increase until β=0.8 was observed. The propulsion velocity decreased again with further rise in β. Further, the number of strokes expended to attain a steady velocity were 70 and 20 (approximately) for β=0.2 and 1, respectively. Even though the thrust generated at commencement of plunging is very high at β=1, however, it fails in sustaining the momentum over time leading to a relatively lower velocity. This phenomenon is analogous to that observed in the flight of birds where larger plunging amplitudes are employed when taking-off from a perched position possibly to minimize the number of strokes needed to attain a significant velocity (Shyy et al., 1999). Similarly, smaller amplitudes are likely employed to gain speed without the limitation of number of strokes required to attain cruising conditions (Alexander, 2002).

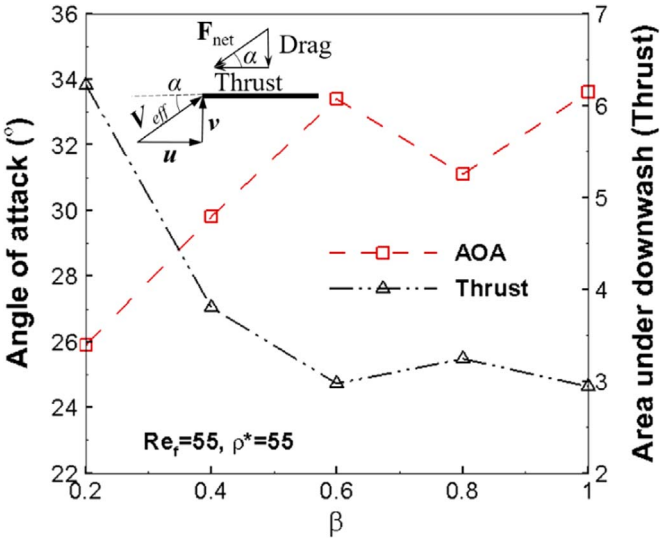

Fig. 14. Time-averaged angle of attack (AOA) and dimensionless downwash for β = 0.2, 0.6, 0.8 and 1 at Re_f=55 with ρ^* = 55. Here y_m is the mean vertical position of the plate. With the cycle-averaged thrust being zero for all β, the time-period for averaging downwash was chosen to be $T/8$. This was done as the instantaneous thrust coefficients dropped from maximum to near zero for this chosen time duration and yielded a meaningful comparison.

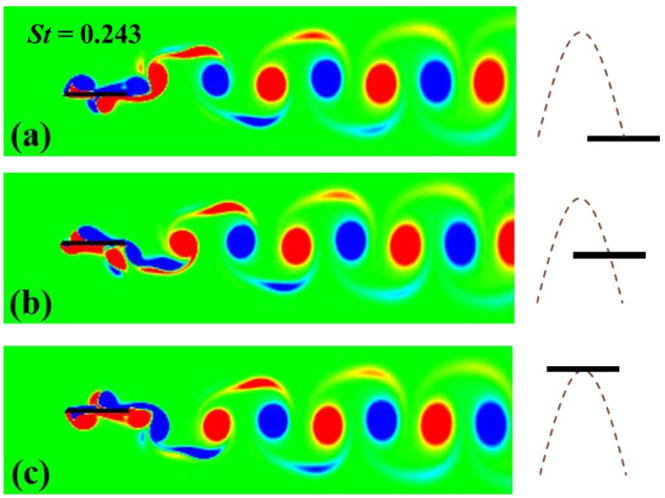

Fig. 15. Wake patterns at cruising condition for a flat plate plunging at β=0.2 with ρ^*=55 and Re_f=55. The right column shows the instantaneous positions and the trajectory during one cycle. Red and blue colors indicate anti-clockwise (out of the plane of pater) and clockwise rotation (into the plane of paper), respectively.(For interpretation of the references to color in this figure,the reader is referred to the web version of this article.)

To identify the reasons for non-monotonous behavior of propulsive velocity with increasing β, the angle of attack and downwash for different β are compared in Fig. 14. The average angle of attack (AOA) for the self-propelled plate was calculated as $\bar{\alpha} = \int_t^{t+\overline{T}} \alpha \, d(t/\overline{T})$, where $\alpha = \tan^{-1}(v/u)$ is the instantaneous angle of attack and $\overline{T} = T/2$. Thus, a higher thrust is expected to result in a higher cruising velocity leading to a smaller inclination with the flight direction. It is well known that jet formation behind a wing generates an opposite reaction force (Arora et al., 2014) and the downwash represents the amount of thrust generated (Freymuth, 1990; Lai and Platzer, 2000). As shown in Fig. 14, AOA and downwash increase and decrease, respectively, when $0.2 \le \beta \le 0.6$. However, AOA decreases (as downwash increases) at $\beta = 0.8$ due to constructive wing-wake interaction at the trailing edge resulting in an increase in the propulsion velocity at this amplitude. This peculiar behavior of decrease in AOA and increase in thrust at β=0.8 attributed to wing-wake interaction is explained further in the following discussion.

The primary cause for high propulsion velocity and thrust at β=0.2 can be understood by scrutiny of the flow patterns and force history. Fig. 15 shows the wake structures at cruising condition for β=0.2 with Re_f=55 and ρ^*=55. As shown in

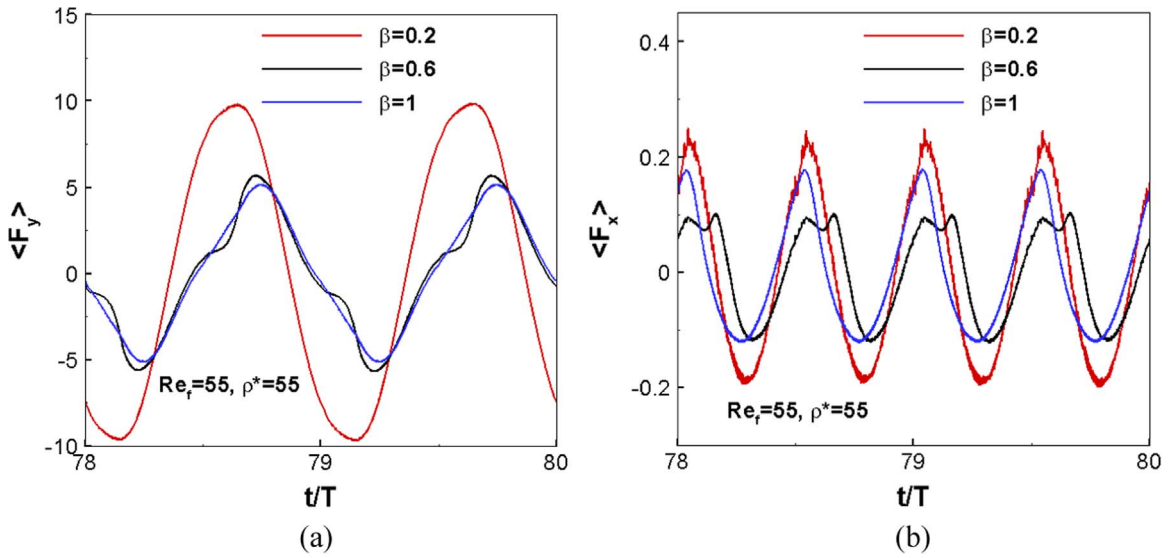

Fig. 16. Time variation of (a) drag and (b) thrust force coefficients for different β with Re_f = 55and ρ^* = 55 at cruising conditions.

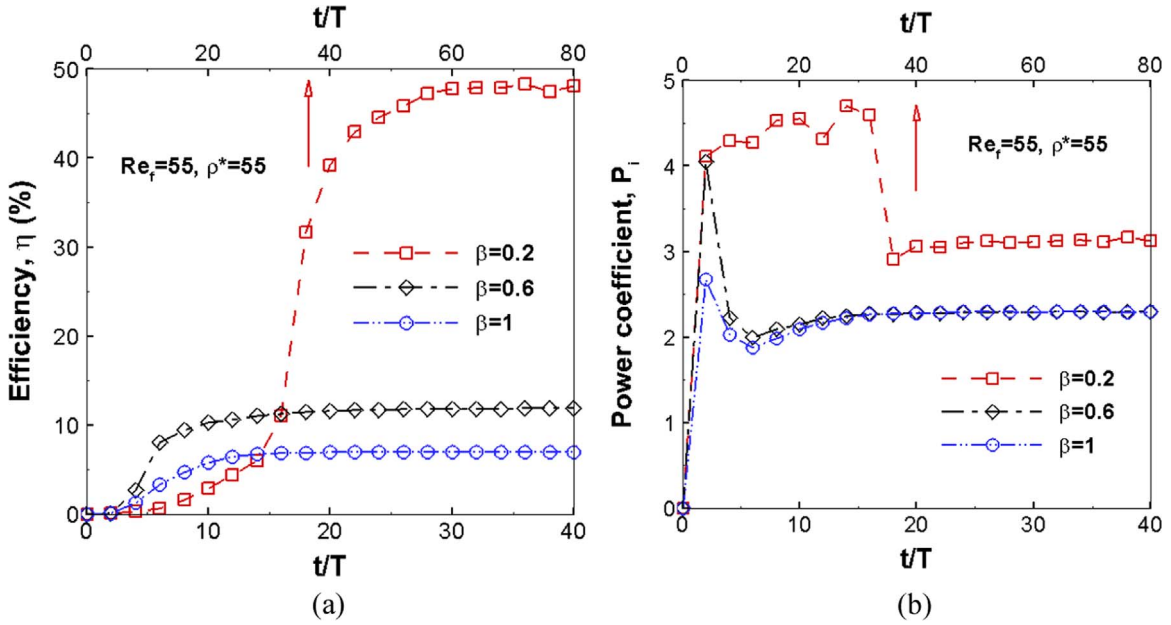

Fig. 17. Cycle-averaged efficiency and input power coefficient for different β with Re_f = 55 and ρ^* = 55. The top and bottom horizontal axis represent the time scales for β=0.2 and β=0.6 and 1, respectively.

this figure, the vortex shedding behavior is very distinct from the patterns shown earlier for different Re_f and with β=0.6. With β=0.2, the separation between the two opposite rotation vortices (one each during upstroke and downstroke) shed per stroke is a minimum. As can be observed from Fig. 15, stroke reversal occurs before the detached LEV could navigate to the trailing edge or is swept away from the plate completely. At the beginning of upstroke the LEV was attached to the plate which created a zone of low pressure at the leading edge. Simultaneously, a strong vortex dipole existed at the trailing edge. The presence of these opposite rotation vortices at the trailing edge assisted in creating a pressure imbalance across the chordwise direction. This pressure differential reflects in the form of a relatively larger thrust for β=0.2, as is indicated in the force coefficients shown in Fig. 16. Another important point to note from this figure is that the drag and thrust coefficients are the highest for β = 0.2. However, the drag coefficient decreases and becomes nearly similar for β = 0.6 and 1. On the other hand, the thrust coefficient decreases till β = 0.6 and increases thereafter.

This behavior of forces due to a high degree of wing–wake interaction echoes in the cycle-averaged efficiency and power coefficients that are shown in Fig. 17. This figure highlights two aspects: (i) the cruising efficiency is highest for low β, and (ii) although a large change in power coefficient is observable when β changes from 0.2 to 0.6, no substantial change can be noticed when it increases from 0.6 to 1. Consequently, the behavior of input power is analogous to that of propulsion velocity which was shown in Fig. 13.

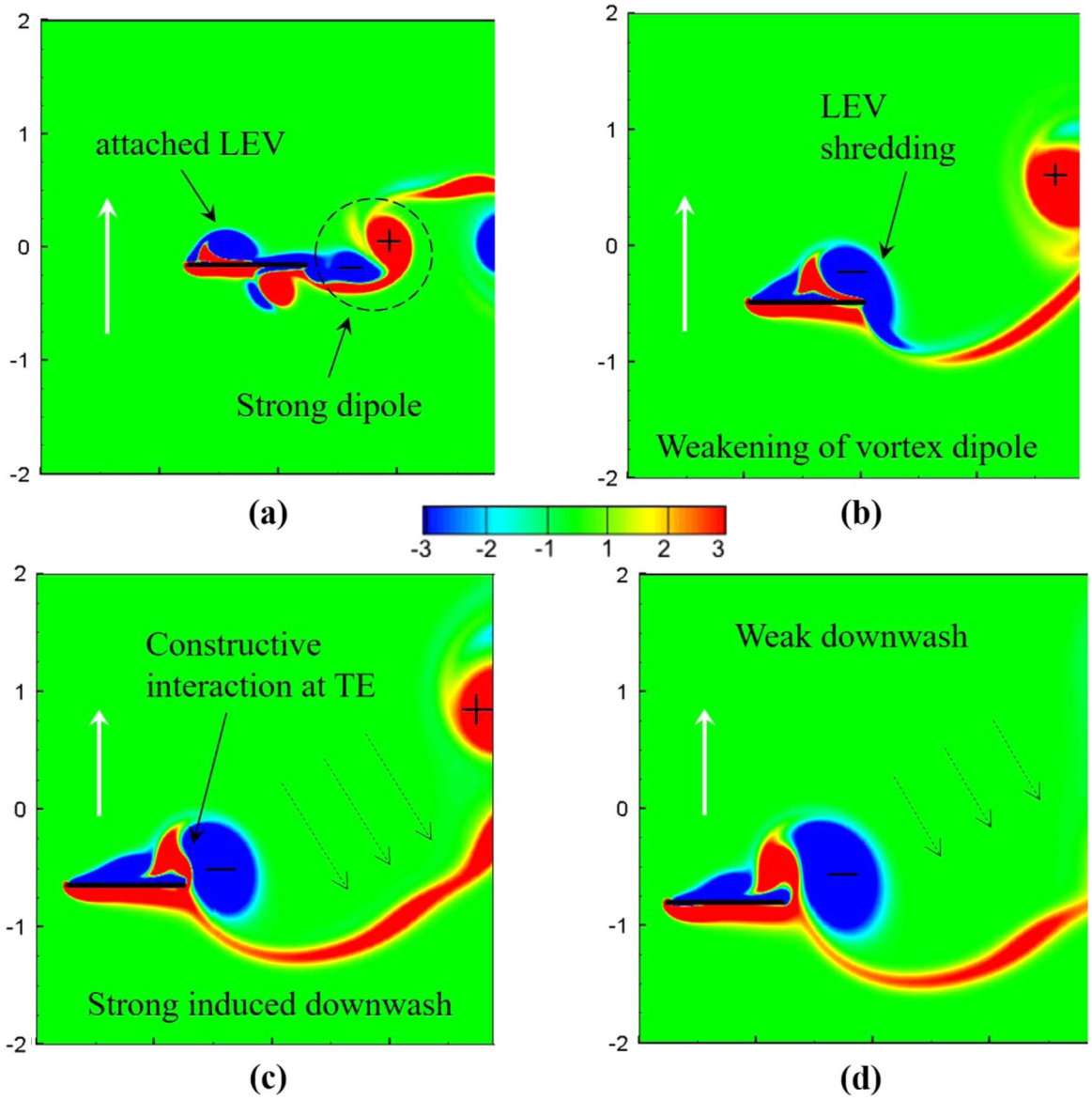

Fig. 18. Flow field around the wing demonstrating induced downwash at t/T=1/10 for (a) β = 0.2, (b) β = 0.6, (c) β = 0.8 and (d) β = 1.0 with Re_f = 55 and ρ^*=55. The white arrows show the direction of movement of the plate.

The increase in thrust between $\beta=0.6$ to $\beta=0.8$ was further investigated by examination of the vortex pattern around the plate and the formation of vortex dipoles at the chosen amplitudes. As is shown in Fig. 18, for $\beta=0.6$ it can be observed that the shed LEV is sheared at the trailing edge by the ascending wing during stroke reversal. Due to this phenomenon, forward momentum is slightly hampered due to the weakening of vortex dipoles as the thrust coefficient and propulsion velocity decrease. On the other hand, for $\beta=0.8$ the shed LEV interacts with the wing exactly at the trailing edge. This shed LEV has enough time to completely advect downstream thereby inhibiting vortex shearing at the trailing edge, providing the desired impetus to propel the plate faster and is indicative of greater area under downwash profile. On the other hand, for $\beta=1$ the LEV grows to such an extent that on shedding there is little interaction with the wing. As the amplitide is highest, the vortices with conflicting rotations are very distant from the trailing edge and the induced downwash due to these dipoles is weak. Thus, the orientation and position of vortices during wing-wake interaction influences the generated thrust. Although reported in reference to 'clap and fling' (Arora et al., 2014), our assessment is that this is the only work in which the effect of wing-wake interaction with respect to induced downwash and strength of vortex dipole has been revealed which leads to increase or decrease in thrust.

Another important observation is that the separation between vortices increases with rise in β. Jones et al. (1998) stated that the wavelength of vortex shedding is inversely proportional to reduced frequency k (where $k=\frac{\gamma C}{\bar{u}}=\frac{St}{2\beta}$). Since the reduced frequency is inversely proportional to β, this justifies the increase in distance between oppositely directed vortices

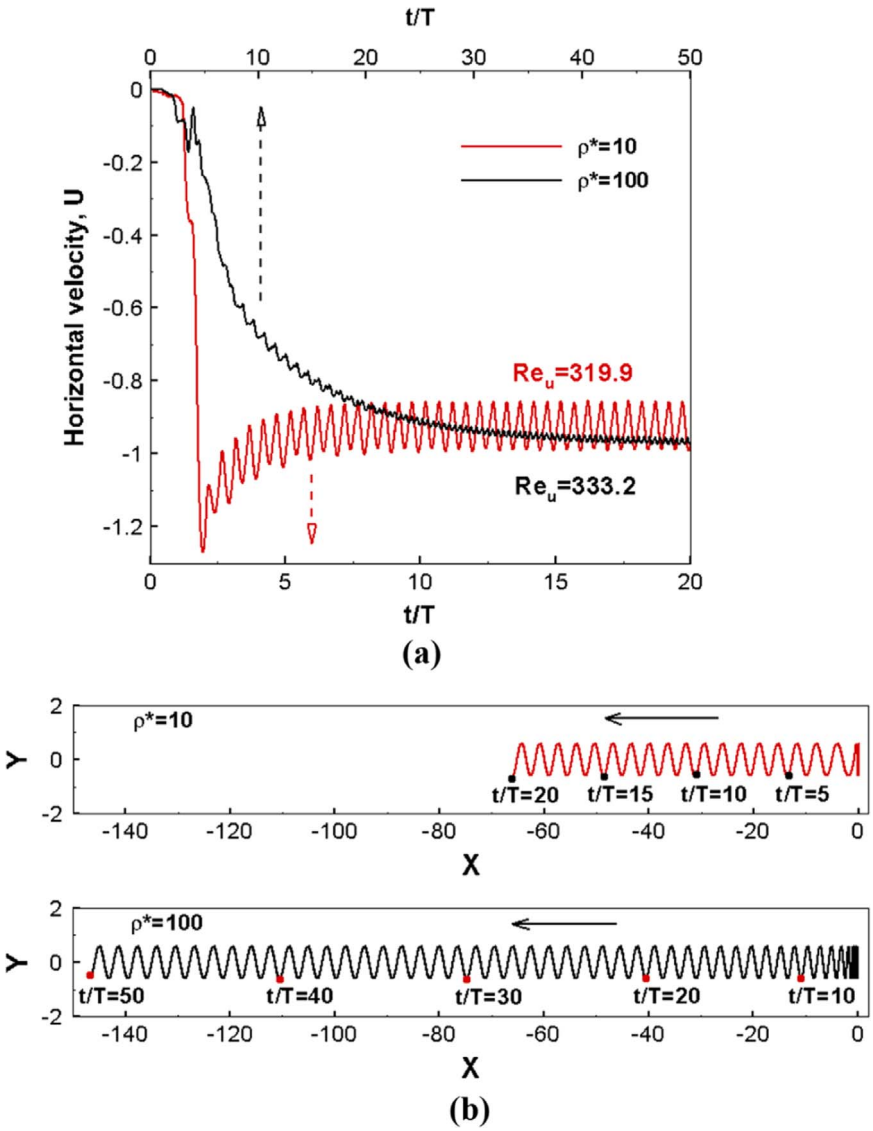

Fig. 19. Comparison of (a) dimensionless instantaneous velocity and (b) non-dimensionalized trajectory for the flat plate plunging at $\rho^*=10$ and 100 with $Re_f=55$ and $\beta=0.6$ when starting from a state of rest. Also shown as dots are the distances reached at the end of specific strokes for the two density ratio situations. By virtue of the plate's higher inertia, the undulations in the velocity are much lower at higher density ratio. Moreover, it takes much longer for a higher inertia plate to reach cruising condition.

with increase in plunging amplitude. For the four cases shown in Fig. 18, the reduced frequencies are (a) $k=0.61$, (b) $k=0.43$, (c) $k=0.19$ and (d) $k=0.16$.

4.3.3. Effect of density ratio (ρ^*)

The effect of density ratio ρ^*, with Re_f and β held fixed, on the propulsion velocity and efficiency-power characteristics is presented in this section. Fig. 19 shows a comparison of the time-evolution of velocity for $\rho^*=10$ and $\rho^*=100$ with $Re_f=55$ and $\beta=0.6$. Also shown are the trajectories of the plate for the two inertia cases. The results show that it takes more number of strokes for the case of the higher inertia system to reach cruising condition. As shown in part (b) of this figure, a higher inertia body is slow to 'react' to the fluid forces and hence lags in the distance covered in the same number of strokes. However, the magnitude of velocity at cruising is nearly the same. Fig. 19 (b) also shows that the cruising velocity is attained after the plate has traversed distances of 68C and 147C for $\rho^*=10$ and 100, respectively. Finally, the undulations in the velocity decrease with increase in density ratio by virtue of the plate's increasing inertia.

The role of plate inertia on aerodynamic force coefficients is depicted in Fig. 20. It can be observed that the magnitudes and evolvement of transverse forces with time are identical and indistinguishable. In addition, no difference in the flow field behavior with change in ρ^* was witnessed, which supported the above argument. These reasons affirm that the drag coefficient is independent of ρ^*; however, the thrust coefficient shows dependence only for lower values of this parameter.

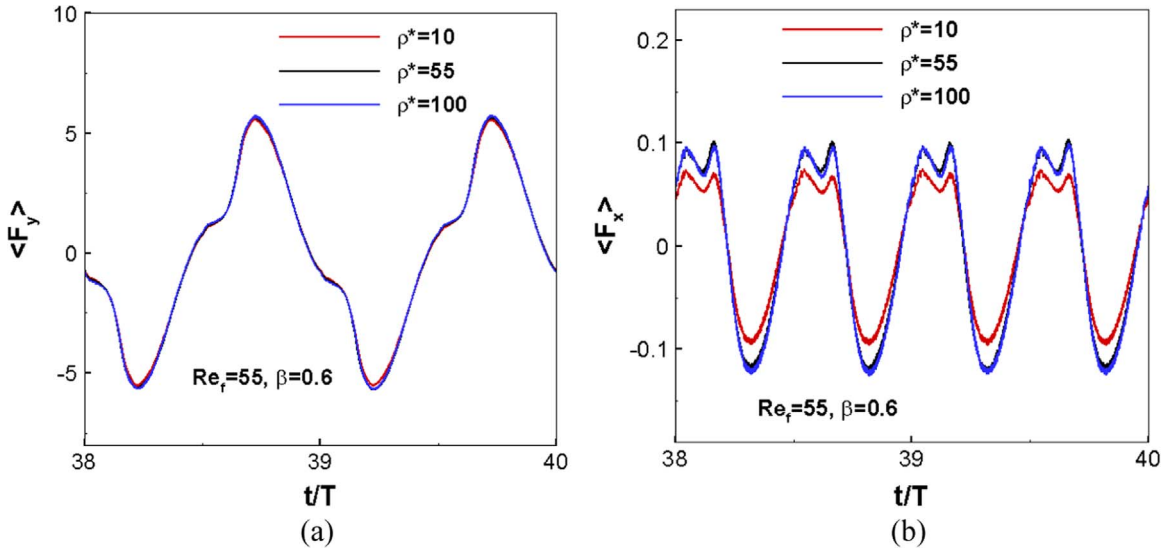

Fig. 20. Time variation of (a) drag and (b) thrust force coefficients for different ρ^* with Re_f = 55and β = 0.6 at cruising conditions.

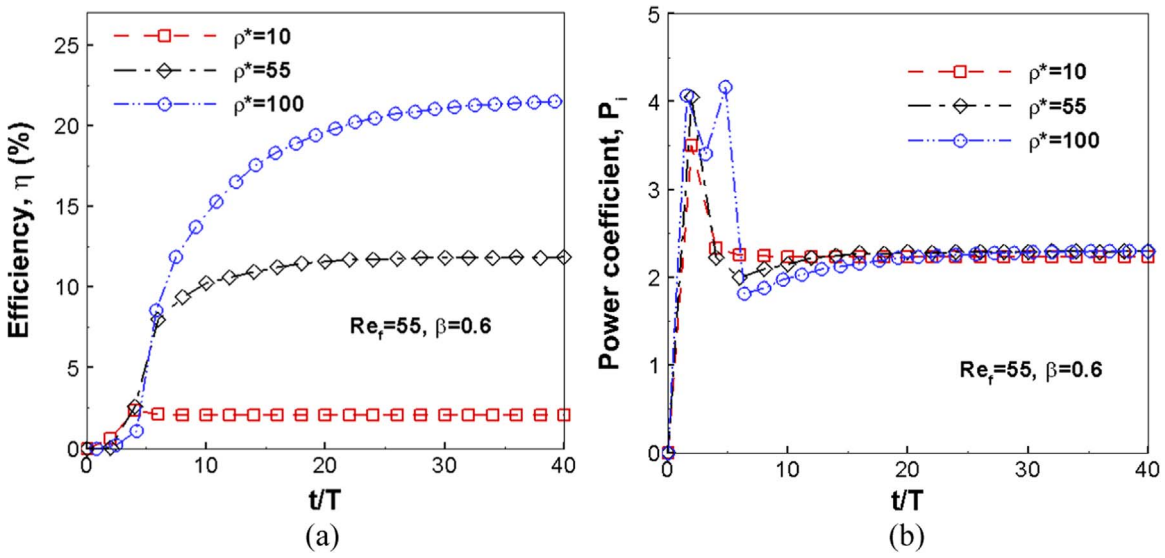

Fig. 21. Cycle-averaged efficiency and input power coefficient for different $\rho^*$with Re_f = 55 and β = 0.6.

These results are unlike those for Re_f and β that were shown earlier. As the drag coefficient and cruising velocity show weak dependence on density ratio, it can be expected that the power coefficient should also be independent of ρ^*. This is corroborated in Fig. 21 which shows the cycle-averaged efficiency and power coefficients for various ρ^*. On the other hand, the cycle-averaged efficiency can be observed to be increasing with increase in ρ^*. Although not so apparent, the non-dimensionalization method for efficiency and power coefficient used in this work can be shown to lead to two inferences to support this data as well; i.e., (a) the cycle-averaged power coefficient does not depend on ρ^*, and (b) the efficiency is proportional to ρ^*. However, this behavior is only valid when a cruising condition is attained. Prior to it, and as shown in Fig. 22, a larger initial effort is required to propel a higher inertia body into locomotion. This figure shows that the area under the $P_i - t/T$ curve i.e. measure of the total work done to reach cruising condition increases with ρ^*. Lighter bodies are expectedly more sensitive to fluid forces and hence respond to even small magnitude oscillations or disturbances, thereby reaching crusing conditions in a lesser number of strokes. On the other hand, higher inertia bodies are less susceptible to flow disturbances and variations and provide a relatively stable cruising velocity that is itself reached by expending greater work.

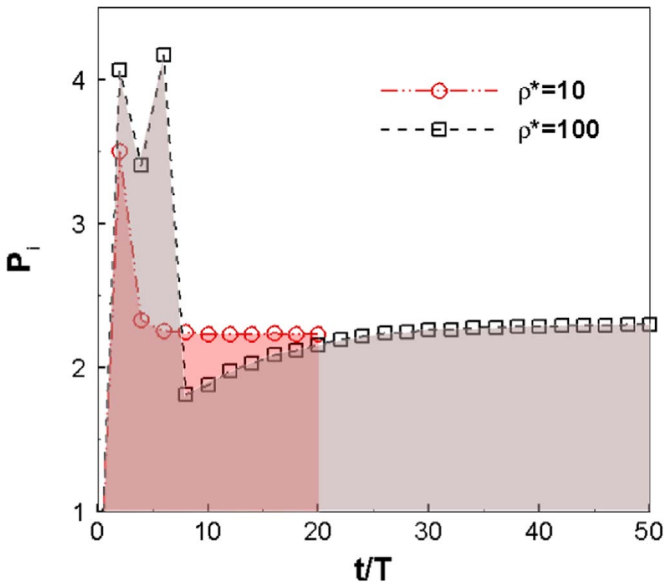

Fig. 22. Comparison of area under the instantaneous power curve (which represents dimensionless work) expended to reach the cruising condition starting from rest at $\rho^*=10$ (red) and $\rho^*=100$ (gray) with $Re_f=55$ and $\beta=0.6$.(For interpretation of the references to color in this figure,the reader is referred to the web version of this article.)

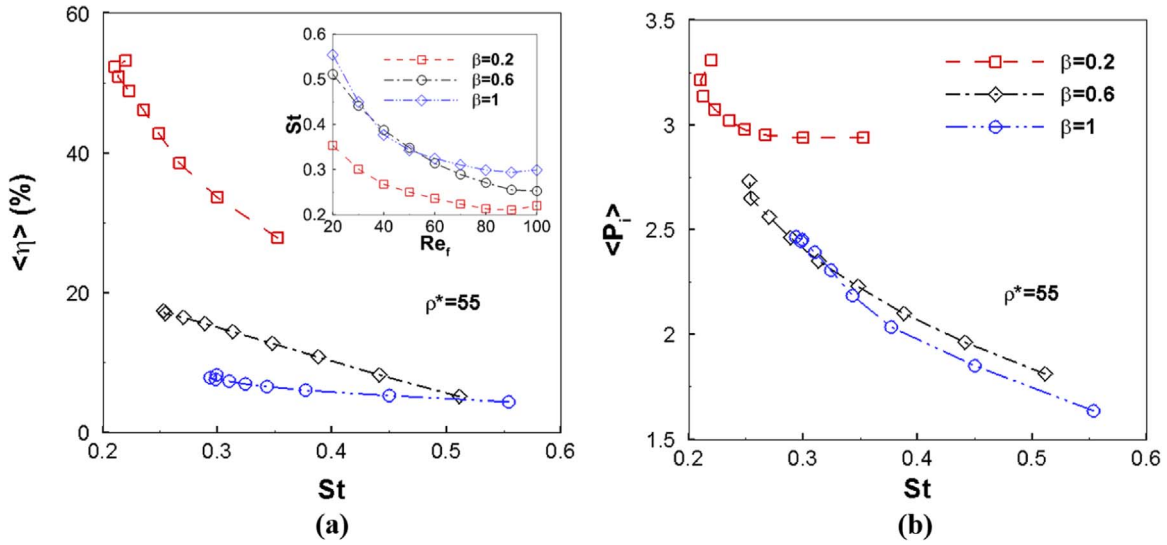

Fig. 23. Variation in cruising (a) propulsion efficiency $<\eta>$ and (b) input power coefficient $<P_i>$ with change in Re_f at $\beta = 0.2$, 0.6 and 1 with $\rho^* = 55$. Inset in (a) shows the behavior of *St* versus Re_f at same parameters.

4.4. Surrogate analysis

So far, an overview of the mechanism of propulsion of a rigid flat plate starting from a state of rest and plunging in a quiescent fluid along with the flow structures, pressure distribution around the plate and force histories had been presented. The time-variation of efficiency and power was also highlighted. To understand the global response and determine the global influence of kinematic parameters, we emphasize the surrogate modelling framework pursued in this work to assess their impact on input power and efficiency.

An initial DOE based upon the parameter range (refer Table 2) was built with 33 training points (15 using FCCD and 18 using LHS). Using the formulated surrogates, however, the $PRESS_{RMS}$ for $<\eta>$ varied from 14% to 25% with Kriging and PRS reduced-order models. The $PRESS_{RMS}$ for $<P_i>$ fared much worse with its range between 70–80%. A careful analysis showed that the model fidelity was very poor for $10 \le \rho^* \le 25$ and $0.6 \le \beta \le 1$. Consequently, the DOE was further refined by including 22 new LHS sampling points such that sampling was significantly improved in the aforementioned range of ρ^* and β. With these 55 training points, the $PRESS_{RMS}$ with 3rd degree PRS for both $<P_i>$ and $<\eta>$ reduced to 4.84% and 2.12%, respectively. The accuracy of the constructed surrogates was further tested by taking 5 random test points where the surrogate predictions were compared to numerical model and the root mean square test errors were recorded to be 2.16% and 4.3% for $<\eta>$ and $<P_i>$, respectively. On an average, 40–50 h were required to run each simulation using parallel programming on a 24-core Intel Xeon Phi processor for the large domain size considered in this work. Since these cross-validation and test errors were less than 5%, the model was considered to have attained satisfactory fidelity. The formulated surrogates were frozen to conduct further analyses. The polynomial expression obtained through surrogate modelling for $<\eta>$ and $<P_i>$ are given in Appendix which had the goodness of fit R_{adj}^2 as 0.996 and 0.977, respectively.

Similar to $<\eta>$ and $<P_i>$, a surrogate model for Strouhal number based on the second-order kriging spline correlation with the same DOE and a $PRESS_{RMS}$ of 4.6% was also formulated. Since this study has been performed on a self-propelled wing, the forward translational velocity or Strouhal number is dependent on the plunging parameters and cannot be varied independently (unlike studies in which the wing flapped at a fixed position where St could be varied by changing the speed of oncoming flow). Therefore, this kriging model enabled us to examine the behavior of $<\eta>$ and $<P_i>$ as a function of St as is shown in Fig. 23. The inset shows the variation in St with Re_f at $\rho^*=55$ and $\beta=0.2$, 0.6 and 1. Although there is a direct relationship between Strouhal number and flapping Reynolds number ($St = 2Re_f/Re_u$), St decreased continuously with increase in Re_f. This is reflected in the continuous increase in efficiency with a decrease in St, with the relationship being nearly linear for higher values of β. Likewise, input power shows a rapid increase with decreasing St (except at $\beta=0.2$, where a sharp change is obtained when St approaches 0.2). In addition, Taylor et al. (2003) stated that flying animals are naturally calibrated to cruise at a Strouhal number lying between 0.2 and 0.4 for efficient flight. Analogous to this finding, 85% of the cases (from simulations and surrogate model) exhibited Strouhal numbers that fell in the efficient flight range (also evident in Fig. 23). The remaining cases where St was off-limit lied in the threshold region (high β, low ρ^* and $Re_f \sim 20$) that represented the transition phase from unsteady to steady propulsion velocity (i.e. aperiodic to periodic vortex shedding). This transition zone was characterized by a deflective wake pattern and which has been discussed in an earlier section.

4.5. Sensitivity analysis

A sensitivity analysis was also performed using the formulated surrogate models. Fig. 24 shows the sensitivity indices of the kinematic parameters on efficiency and input power. The main sensitivity index quantifies the direct influence of

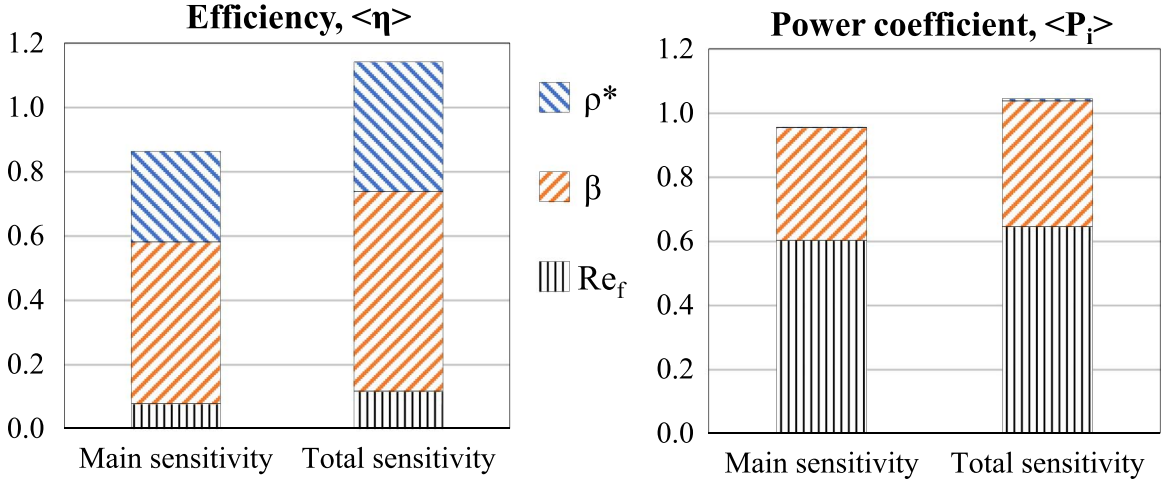

Fig. 24. Global sensitivity analysis of efficiency $<\eta>$ and power coefficient $<P_i>$ showing main and total sensitivity indices.

individual parameters on the change in dependent variable, whereas the total index specifies the joint or collective impact of the input variables on the objective function. The deficit of these two indices is a measure of the cross interaction or the interconnectivity of the parameters.

The sensitivity analysis of efficiency showed that β is the most influential parameter, with its main index being largest amongst all the three variables. Moreover, β and ρ^* had a coupled effect as together they had a significant impact on efficiency. This is clearly noticeable in the total sensitivity indices of β and ρ^* which are higher than their main counterparts by about 12.5%, implying the extent of interaction of these two variables is quite significant (for Re_f, there was only a marginal increase in total sensitivity of mere 3%). On the contrary, Re_f does not influence efficiency as much as other kinematic parameters.

As far as the input power coefficient is concerned, Re_f had the maximum sensitivity index making it to be the most dominant parameter. The sensitivity analysis also confirms the earlier argument of insignificant effect of density ratio. Nevertheless, ρ^* could not be ignored as the sensitivity analysis of efficiency established it to be a crucial parameter as well.

4.6. Pareto front

In multi-objective problems with several variables, the optimization process does not involve a single solution but multiple designs that minimize or maximize the objectives simultaneously. Thus, the locus of dominating or superior points representing this behavior (trade-off region between minima of conflicting objectives) is known as the Pareto-front or optimal solutions (Trizila et al., 2011; Miettinen, 1999). Since Pareto-front evaluation involves the minimization of all objective functions, the quantity to be maximized is usually multiplied by negative one.

In this work, the focus is towards identifying conditions for which the highest propulsion efficiency with the minimum power requirements can be achieved. The entire design space was probed by partitioning the range of Re_f, ρ^* and β into equal number of levels to generate the values of efficiency and input power using the developed PRS surrogate models. Thereafter, the optimal or dominating points that constitute the Pareto-front were extracted using a multi-objective optimization tool in MATLAB®. As shown in Fig. 25, there is a large set of non-dominated or inferior points (characterized by red symbols) with the Pareto-front acting as the periphery where none of the objectives could be enhanced together. These Pareto-front points were spread across all Re_f but with $\rho^* \sim 80$–100 and represent the operating conditions where maximum propulsion efficiency is achievable. The shaded region shown in the figure comprises of non-dominating points and typifies the zone of propulsion, i.e., conditions under which propulsion, though not necessarily the most efficient, will be the outcome. The filled circles (black) denote the efficiency and input power for the set of training points of the DOE that

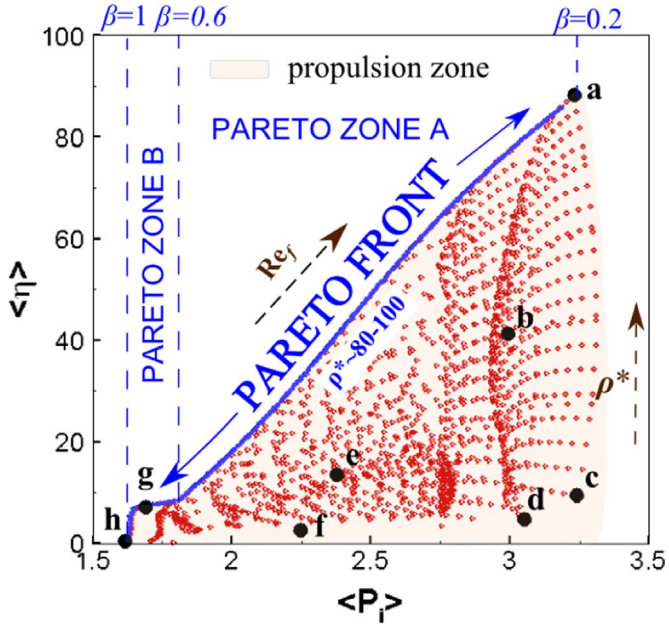

Fig. 25. Pareto-front optimization for input power and efficiency at cruising condition. The symbols (red) are data obtained from the constructed surrogate models with the Pareto-front being the set of dominating points. Thus, the Pareto-front provides the locus of flow scenarios where the maximum efficiency for a given input power can be realized. For the same input power coefficient, efficiency is higher for a higher inertia system, with the maximum reached near the highest ρ^*considered in this work. On the Pareto-front, efficiency increases with increasing Re_f and decreasing β. 'Zone A' is defined for low to intermediate amplitudes (i.e., $0.2 \le \beta \le 0.6$) while 'Zone B' for intermediate to high amplitudes (i.e, $0.6 \le \beta \le 1$). The parametric coordinates of the filled circles (black) are: (a) $\mathrm{Re}_f = 100$, $\rho^* = 100$, $\beta = 0.2$, (b) $\mathrm{Re}_f = 20$, $\rho^* = 100$, $\beta = 0.2$, (c) $\mathrm{Re}_f = 100$, $\rho^* = 10$, $\beta = 0.2$, (d) $\mathrm{Re}_f = 20$, $\rho^* = 10$, $\beta = 0.2$, (e) $\mathrm{Re}_f = 100$, $\rho^* = 100$, $\beta = 1$, (f) $\mathrm{Re}_f = 100$, $\rho^* = 10$, $\beta = 1$, (g) $\mathrm{Re}_f = 20$, $\rho^* = 100$, $\beta = 1.0$ and (h) $\mathrm{Re}_f = 20$, $\rho^* = 10$, $\beta = 1$.(For interpretation of the references to color in this figure,the reader is referred to the web version of this article.)

correspond to FCCD sampling. The maximum and minimum propulsion efficiency are obtained at **a** ($Re_f = 100$, $\rho^* = 100$, $\beta = 0.2$) and **h** ($Re_f = 20$, $\rho^* = 10$, $\beta = 1$), respectively, which lie at the diagonally opposite corners of the DOE.

As is shown in the figure, a key outcome from an analysis of the Pareto-front is that the set of optimal points could be split into two zones, A & B. 'Zone A' corresponds to low to intermediate amplitudes, while 'zone B′ is for intermediate to high amplitudes. Further, parametric analysis shows that high efficiency, though with requirement of large input power, is achievable in zone A while zone B can only yield scenarios corresponding to low input power and efficiency. This Pareto-front indicates that the best efficiency can be achieved only in high inertia systems by increasing both the flapping Reynolds number and decreasing the amplitude ratio, though at the expense of greater input power. Clearly, wing-wake interaction which occurs due to weaker vortex dissipation at high Re_f and presence of vortex dipole at the trailing edge at low amplitudes acting in tandem can lead to achievement of high propulsion efficiency.

5. Conclusions

The present work was directed towards characterizing the fluid mechanics associated with a self-propelled-heaving rigid flat plate in a quiescent medium. In this regard, a shifting discontinuous-grid-block around a moving solid body based on the multi-relaxation time lattice Boltzmann method was employed. A parametric study was performed to characterize the influence of Reynolds number Re_f, plunging amplitude β and density ratio ρ^* on the forward flight efficiency and power requirements for the flat plate at cruising conditions. In addition, the impact of these variables on propulsion velocity was elucidated with the help of flow structures and their interaction with the wing.

Simulations exhibited that attainment of cruising condition resulted in a periodically varying thrust coefficient that owed this behavior to the pressure at leading and trailing edges alternating between maximum and minimum values. This was shown to depend on the kinematics and occurred due to opposite-orientation vortices getting shed during upstroke and downstroke. Various periodic vortex shedding characteristics of the plunging plate were observed that led to modification of the angle of attack as a result of wing-wake interaction and downward jet.

It was also revealed that with increase in flapping Reynolds number (Re_f), the propulsion velocity (or Re_u), cruising efficiency and input power coefficient increased due to an increased degree of wing-wake interaction. At low Re_f, vortices were shed at an angle (indicative of transition phase from unsteady to quasi-steady propulsion) which quickly dissipated, whereas at high values of Re_f a long, equally spaced and oppositely directed symmetric trail was observed. At low β, a strong vortex dipole prevailed at the trailing edge along with an attached LEV that led to maximum thrust generation and highest cruising efficiency. For higher β, the position and orientation of vortices during stroke reversal dictated the productive or destructive effect of wing-wake interaction leading to an increase or decrease in the angle of attack and downwash. For the density ratio (ρ^*), the overall energy expended to attain a cruising condition starting from rest was much higher for higher inertia bodies as a larger number of plunging strokes was required to reach this stage. Lastly, cruising efficiency increased with increase in ρ^* as it became directly proportional to wing inertia.

Surrogate modelling was employed to assess and identify the optimum conditions for forward flight. Based on the formulated surrogate models of efficiency and input power requirements for forward flight, a Pareto-optimal solution which described the tradeoff between these two competing objectives was obtained. The Pareto-front analysis highlighted that the set of optimal points could be split into two zones corresponding to low and high amplitude kinematics. This Pareto-front indicated that wing-wake interaction which occurs at low β and high Re_f due to weak vortex dissipation and presence of vortex dipole at the trailing edge acting in tandem can lead to achieving high propulsion efficiency in high inertia systems. This Pareto-front provided guidance on the maximum efficiency that can be attained for a given input power, thereby defining the ideal operating range and is expected to be of significance for the design of next generation flapping wing MAVs.

Acknowledgement

N.A. and A.G. acknowledge the financial support received from the Aeronautics Research and Development Board (ARDB) under SIGMA project No. 1705. The authors also thank the IIT Delhi HPC facility for computational resources.

Appendix

Multi-Relaxation Time LBM

In this method, the distribution function f (as defined in the SRT model) in the discrete velocity space **F** is mapped onto the moment space **K** by using a transformation matrix M (Arora et al., 2016), i.e.

$$\hat{f} = Mf \text{ and } f = M^{-1}\hat{f} \tag{25}$$

where $\hat{\hat{f}}$ is a column matrix consisting of moments of the velocity distribution function (each row vector) which represents the following quantities in two-dimensional space:

$$\hat{\hat{f}} = \left[\rho, e, \varepsilon, j_x, q_x, j_y, q_y, p_{xx}, p_{xy}\right]^T \tag{26}$$

where ρ is the density, e signifies the kinetic energy, ε epitomizes the square of kinetic energy, j_x and j_y are the x and y components of the momentum flux, q_x and q_y are related to the x and y components of energy density, and p_{xx} and p_{xy} refer to the diagonal and off-diagonal terms in viscous stress tensor.

The equilibrium values for the non-conserved moments can be obtained from the conserved moments ρ and $\boldsymbol{j}$ (j_x and j_y) (Arora et al., 2016) as

$$e^{eq} = -2\rho + \frac{3}{\rho}\left(j_x^2 + j_y^2\right) \tag{27}$$

$$\varepsilon^{eq} = \rho - \frac{3}{\rho}\left(j_x^2 + j_y^2\right) \tag{28}$$

$$q_x^{eq} = -j_x \quad , \quad q_y^{eq} = -j_y \tag{29}$$

$$p_{xx}^{eq} = \frac{1}{\rho}\left(j_x^2 - j_y^2\right) \tag{30}$$

$$p_{xy}^{eq} = \frac{1}{\rho} j_x j_y \tag{31}$$

The transformation matrix for the D2Q9 model is given by Arora et al. (2016)

$$M = \begin{bmatrix} 1 & 1 & 1 & 1 & 1 & 1 & 1 & 1 & 1 \\ -4 & -1 & -1 & -1 & -1 & 2 & 2 & 2 & 2 \\ 4 & -2 & -2 & -2 & -2 & 1 & 1 & 1 & 1 \\ 0 & 1 & 0 & -1 & 0 & 1 & -1 & -1 & 1 \\ 0 & -2 & 0 & 2 & 0 & 1 & -1 & -1 & 1 \\ 0 & 0 & 1 & 0 & -1 & 1 & 1 & -1 & -1 \\ 0 & 0 & -2 & 0 & 2 & 1 & 1 & -1 & -1 \\ 0 & 1 & -1 & 1 & -1 & 0 & 0 & 0 & 0 \\ 0 & 0 & 0 & 0 & 0 & 1 & -1 & 1 & -1 \end{bmatrix} \tag{32}$$

The collision process is performed in the **K** space which is as follows:

$$\hat{\hat{f}}_* = \hat{\hat{f}} - S\left[\hat{\hat{f}} - \hat{\hat{f}}^{eq}\right] \tag{33}$$

Table 4
Third-degree polynomial coefficients obtained from surrogate modelling for $<\eta>$ and $<P_i>$.

Coefficient	$\langle\eta\rangle$	$\langle P_i\rangle$
a_0	4.55	3.05
a_1	20.93	−0.50
a_2	49.24	−0.16
a_3	−33.98	−5.63
a_4	−19.84	0.71
a_5	56.72	1.13
a_6	−32.30	3.27
a_7	1.62	−0.23
a_8	−119.78	−0.19
a_9	74.62	9.27
a_{10}	3.82	−0.03
a_{11}	−16.63	−0.45
a_{12}	19.78	−1.52
a_{13}	1.99	−0.62
a_{14}	−37.78	−0.01
a_{15}	9.81	−1.30
a_{16}	−14.15	0.33
a_{17}	17.22	−0.14
a_{18}	72.52	0.47
a_{19}	−44.80	−5.07

where $\hat{f}_*$ is the post collision operator, and S is the diagonal relaxation time matrix

$$S = diag[s_1, s_2, s_3, s_4, s_5, s_6, s_7, s_8, s_9] \tag{34}$$

where $s_1 = s_4 = s_6 = 0$ (relaxation time for the conserved quantities).

The moments $\hat{f}$ are transformed back and thus the advection step is carried out in the **F** space on the distribution function f. Thus, Eq. (33) can be written as

$$\tilde{f} = M^{-1}\hat{f} - M^{-1}S\left[\hat{f} - \hat{f}^{eq}\right] \tag{35}$$

where $\tilde{f}$ is the post collision distribution function in **F** space which are then streamed to the neighboring nodes in direction of the lattice velocities.

6.1. Surrogate model

The 3rd degree polynomial expression for $<\eta>$ and $<P_i>$ is as follows

$$\langle\eta\rangle, \langle P_i\rangle = a_0 + a_1\mathrm{Re_f} + a_2\rho^* + a_3\beta + a_4\mathrm{Re_f}^2 + a_5\mathrm{Re_f}\rho^* + a_6\mathrm{Re_f}\beta + a_7\rho^{*2} + a_8\rho^*\beta + a_9\beta^2 + a_{10}\mathrm{Re_f}^3 + a_{11}\mathrm{Re_f}^2\rho^* + a_{12}\mathrm{Re_f}^2\beta + a_{13}\mathrm{Re_f}\rho^{*2} + a_{14}\mathrm{Re_f}\rho^*\beta + a_{15}\mathrm{Re_f}\beta^2 + a_{16}\rho^{*3} + a_{17}\rho^{*2}\beta + a_{18}\rho^*\beta^2 + a_{19}\beta^3 \tag{36}$$

The coefficients as obtained from the PRS surrogate model for normalized values of Re_f, ρ^* and β (range scaled between 0 and 1) are given in Table 4.

References

Alben, S., Shelley, M., 2005. Coherent locomotion as an attracting state for a free flapping body. Proc. Natl. Acad. Sci. 102, 11163–11166.

Alexander, D.E., 2002. In: Nature's FlyersThe John Hopkins University Press, Baltimore.

Anderson, J.M., Streitlien, K., Barrett, D.S., Triantafyllou, M.S., 1998. Oscillating foils of high propulsive efficiency. J. Fluid Mech. 360, 41–72.

Aono, H., Gupta, A., Qi, D., and Shyy, W., The Lattice Boltzmann Method for Flapping Wing Aerodynamics, In: Proceedings of the 40th AIAA Fluid Dynamics Conference and Exhibit, June 2010, Chicago, Illinois, USA.

Arora, N., Gupta, A., Shyy, W., 2016. A shifting discontinuous-grid-block lattice Boltzmann method for moving boundary simulations. Comput. Fluids 125, 59–70.

Arora, N., Gupta, A., Sanghi, S., Aono, H., Shyy, W., 2014. Lift-drag and flow structures associated with the 'clap and fling' motion. Phys. Fluids 26, 071906.

Benkherouf, T., Mekadem, M., Oualli, H., Hanchi, S., Keirsbulck, L., Labraga, L., 2011. Efficiency of an auto-propelled flapping airfoil. J. Fluids Struct. 27, 552–566.

Betz, A., 1912. Ein Beitrag zur Erklarung des Segelfluges. Zeitsch. Flugtechnik Motorluftschiffahrt 3, 269–272.

Chen, S., Doolen, G.D., 1998. Lattice Boltzmann method for fluid flows. Annu. Rev. Fluid Mech. 30, 329–364.

Chin, D.D., Lentink, D., 2016. Flapping wing aerodynamics: from insects to vertebrates. J. Exp. Biol. 219, 920–932.

Croon, De, G. C. H. E, Percin, M., Remes, B.D.W., Ruijsink, R., De Wagter, C., 2016. The DelFly: Design, Aerodynamics, and Artificial Intelligence of a Flapping Wing Robot. Springer, London.

Dickinson, M.H., Lehmann, F.-O., Sane, S.P., 1999. Wing rotation and the aerodynamic basis of insect flight. Science 284, 1954–1960.

Freymuth, P., 1988. Propulsive vortical signature of plunging and pitching airfoils. AIAA J. 26, 881–883.

Freymuth, P., 1990. Thrust generation by an airfoil in hover modes. Exp. Fluids 9, 17–24.

Fuller, S.B., Karpelson, M., Censi, A., Ma, K.Y., Wood, R.J., 2014. Controlling free flight of a robotic fly using an onboard vision sensor inspired by insect Ocelli. J. R. Soc. Interface 11, 0281.

Goel, T., Dorney, D.J., Haftka, R.T., Shyy, W., 2008. Improving the hydrodynamic performance of diffuser vanes via shape optimization. Comput. Fluids 37, 705–723.

Hu, J., Xiao, Q., 2014. Three-dimensional effects on the translational locomotion of a passive heaving wing. J. Fluids Struct. 46, 77–88.

Jones, K.D., Dohring, C.M., Platzer, M.F., 1998. Experimental and computational investigation of the Knoller–Betz effect. AIAA J. 36, 1240–1246.

Kang, C.K., Shyy, W., 2013. Scaling law and enhancement of lift generation of an insect-size hovering flexible wing. J. R. Soc. Interface 10, 0361.

Kang, C.K., Shyy, W., 2014. Analytical model for instantaneous lift and shape deformation of an insect-scale flapping wing in hover. J. R. Soc. Interface 11, 0933.

Kang, C.K., Aono, H., Cesnik, C.E.S., Shyy, W., 2011. Effects of flexibility on the aerodynamic performance of flapping wings. J. Fluid Mech. 689, 32–74.

Katzmayr, R., Effect of Periodic Changes of Angle of Attack on Behavior of Airfoils, (translated From Zeitschrift fur Flugtechnik und Motorluftschiffahrt, March 31, 1922, pp. 80–82, and April 13, 1922, pp. 95–101.

Keennon, M., Klingebiel, K., Won, H., and Andriukov, A., Development of the Nano hummingbird: A tailless flapping wing micro air vehicle. In: Proceedings of the 50th AIAA Aerospace Sciences Meeting, Reston, Virginia, USA: January 2012.

Kern, S., Koumoutsakos, P., 2006. Simulations of optimized anguilliform swimming. J. Exp. Biol. 209, 4841–4857.

Knoller, R., 1909. Die Gesetze des Liftwiderstandes. Flug- und Motortechnik (Wiener) 3 (21), 1–7.

Ladd, A.J.C., 1994. Numerical simulations of particulate suspensions via a discretized boltzmann equation. Part 1. Theoretical Foundation. J. Fluid Mech. 271, 285–309.

Lai, J.C.S., Platzer, M.F., 2000. Characteristics of a plunging airfoil at zero freestream velocity. AIAA J. 39, 531–534.

Lallemand, P., Luo, L.-S., 2003. Lattice Boltzmann method for moving boundaries. J. Comput. Phys. 184, 406–421.

Lee, J., Choi, H., Kim, H.-Y., 2015. A scaling law for the lift of hovering insects. J. Fluid Mech. 782, 479–490.

Lewin, G.C., Haj-Hariri, H., 2003. Modelling thrust generation of a two-dimensional heaving airfoil in a viscous flow. J. Fluid Mech. 492, 339–362.

Lu, X.-Y., Liao, Q., 2006. Dynamic responses of a two-dimensional flapping foil motion. Phys. Fluids 18, 098104.

Ma, K. Y., Chirarattananon, P., and Wood, R.J., Design and Fabrication of an Insect-scale Flying Robot for Control Autonomy. In: Proceedings of the IEEE/RSJ International Conference on Intelligent Robots and Systems (IROS), Hamburg, Germany: 2015.

Miettinen, K.M., 1999. Nonlinear Multiobjective Optimization, BostonKluwer Academic.

Muller, T.J., 2001. Fixed and flapping wing aerodynamics for micro air vehicle applications. AIAA Prog. Astronaut. Aeronaut, 195.

Quiepo, N.V., Haftka, R.T., Shyy, W., Goel, T., Vaidyanathan, R., Tucker, P.K., 2005. Surrogate-based analysis and optimization. Prog. Aerosp. Sci. 41, 1–28.

Quinn, D.B., Lauder, G.V., Smits, A.J., 2013. Scaling the propulsive performance of heaving flexible panels. J. Fluid Mech. 738, 250–267.

Sane, S.P., 2003. The aerodynamics of insect flight. J. Exp. Biol. 206, 4191–4208.

Schultz, W.W., Webb, P.W., 2002. Power requirements of swimming: do new methods resolve old questions? Integr. Comp. Biol. 42, 1018–1025.

Shyy, W., Berg, M., Ljungqvist, D., 1999. Flapping and flexible wings for biological and micro air vehicles. Prog. Aerosp. Sci. 35, 155–205.

Shyy, W., Papila, N., Vaidyanathan, R., Tucker, K., 2001. Global design optimization for aerodynamics and rocket propulsion components. Prog. Aerosp. Sci. 37, 59–118.

Shyy, W., Trizila, P., Kang, C., Aono, H., 2009. Can Tip vortices enhance lift of a flapping wing? AIAA J. 47, 289–293.

Shyy, W., Aono, H., Kang, C.-K., Liu, H., 2013. In: An Introduction to Flapping Wing AerodynamicsCambridge University Press, New York.

Shyy, W., Lian, Y., Tang, J., Viieru, D., Liu, H., 2008. In: Aerodynamics of Low Reynolds Number FlyersCambridge University Press, New York.
Shyy, W., Kang, C.-k, Chirarattananon, P., Ravi, S., Liu, H., 2016. Aerodynamics, sensing and control of insect-scale flapping wing-flight. Proc. R. Soc. A 472, 20150712.
Shyy, W., Cho, Y.-C., Du, W., Gupta, A., Tseng, C.-C., Sastry, A.M., 2011. Surrogate-based modeling and dimension reduction techniques for multi-scale mechanics problems. Acta Mech. Sin. 27, 845–865.
Shyy, W., Aono, H., Chimakurthi, S.K., Trizila, P., Kang, C.K., Cesnik, C.E.S., Liu, H., 2010. Recent progress in flapping wing aerodynamics and aeroelasticity. Prog. Aerosp. Sci. 46, 284–327.
Succi, S., 2001. In: The Lattice Boltzmann Equation for Fluid Dynamics and BeyondOxford University Press, New York.
Taylor, G.K., Nudds, R.L., Thomas, A.L.R., 2003. Flying and swimming animals cruise at a strouhal number tuned for high power efficiency. Nature 425, 707–711.
Triantafyllou, M.S., Triantafyllou, G.S., Gopalkrishnan, R., 1991. Wake mechanics for thrust generation in oscillating airfoils. Phys. Fluids 3 (12), 1989–1993.
Trizila, P., Kang, C.-K., Aono, H., Visbal, M., Shyy, W., 2011. Low Reynolds number aerodynamics of a flapping rigid flat plate. AIAA J. 49, 806–823.
Tsai, B.-J., Fu, Y.-C., 2009. Design and aerodynamic analysis of a flapping-wing micro aerial vehicle. Aerosp. Sci. Technol. 13, 383–392.
Vandenberghe, N., Zhang, J., Childress, S., 2004. Symmetry breaking leads to forward flapping flight. J. Fluid Mech. 506, 147–155.
Vandenberghe, N., Childress, S., Zhang, J., 2006. On unidirectional flight of a free flapping wing. Phys. Fluids 18, 014102.
Zhang, X., Ni, S., Wang, S., He, G., 2009. Effects of geometric shape on the hydrodynamics of a self-propelled flapping foil. Phys. Fluids 21, 103302.